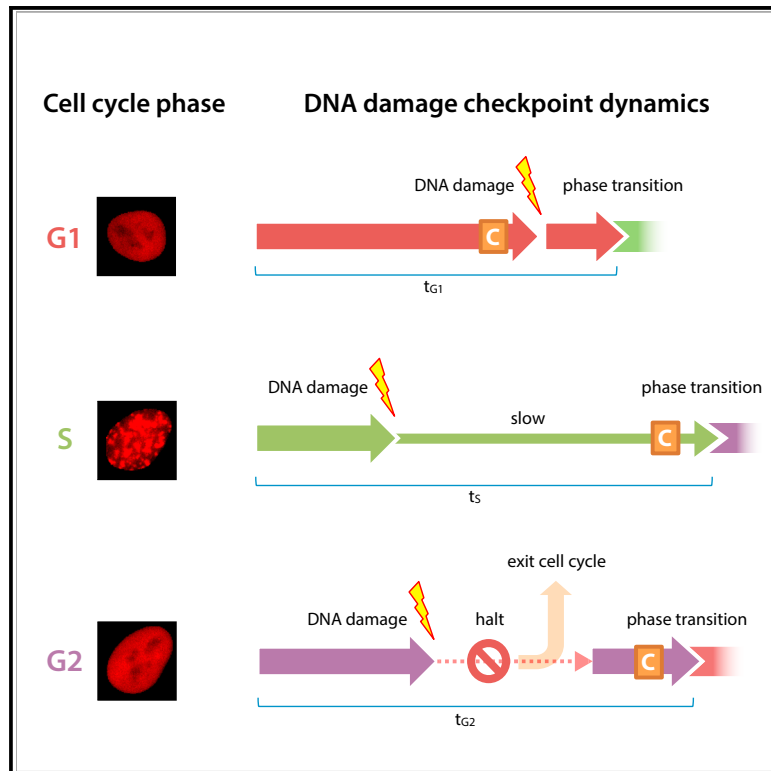


Orchestration of DNA Damage Checkpoint Dynamics across the Human Cell Cycle

Graphical Abstract



Authors

Hui Xiao Chao, Cere E. Poovey, Ashley A. Privette, Gavin D. Grant, Hui Yan Chao, Jeanette G. Cook, Jeremy E. Purvis

Correspondence

jeremy_purvis@med.unc.edu

In Brief

Chao et al. find that each cell-cycle phase shows a distinct sensitivity and temporal response to DNA damage, explaining why differences in the timing of DNA damage can lead to heterogeneous cell fate outcomes.

Highlights

- In gap phases, DNA damage triggers a complete halt to cell-cycle progression
- Damage during S phase slows down progression according to severity
- The duration of arrest during gap phases correlates with damage severity
- The S phase checkpoint is the least sensitive to DNA damage



Orchestration of DNA Damage Checkpoint Dynamics across the Human Cell Cycle

Hui Xiao Chao,^{1,2} Cere E. Poovey,¹ Ashley A. Privette,¹ Gavin D. Grant,^{3,4} Hui Yan Chao,¹ Jeanette G. Cook,^{3,4} and Jeremy E. Purvis^{1,2,4,5,*}

¹Department of Genetics, University of North Carolina, Chapel Hill, Genetic Medicine Building 5061, CB#7264, 120 Mason Farm Road, Chapel Hill, NC 27599-7264, USA

²Curriculum for Bioinformatics and Computational Biology

³Department of Biochemistry and Biophysics

⁴Lineberger Comprehensive Cancer Center, University of North Carolina, Chapel Hill, 120 Mason Farm Road, Chapel Hill, NC 27599-7264, USA

⁵Lead Contact

*Correspondence: jeremy_purvis@med.unc.edu

<https://doi.org/10.1016/j.cels.2017.09.015>

SUMMARY

Although molecular mechanisms that prompt cell-cycle arrest in response to DNA damage have been elucidated, the systems-level properties of DNA damage checkpoints are not understood. Here, using time-lapse microscopy and simulations that model the cell cycle as a series of Poisson processes, we characterize DNA damage checkpoints in individual, asynchronously proliferating cells. We demonstrate that, within early G1 and G2, checkpoints are stringent: DNA damage triggers an abrupt, all-or-none cell-cycle arrest. The duration of this arrest correlates with the severity of DNA damage. After the cell passes commitment points within G1 and G2, checkpoint stringency is relaxed. By contrast, all of S phase is comparatively insensitive to DNA damage. This checkpoint is graded: instead of halting the cell cycle, increasing DNA damage leads to slower S phase progression. In sum, we show that a cell's response to DNA damage depends on its exact cell-cycle position and that checkpoints are phase-dependent, stringent or relaxed, and graded or all-or-none.

INTRODUCTION

The human cell cycle is a complex sequence of molecular events by which cells replicate and segregate their genomic DNA. Cell-cycle progression is restrained by multiple checkpoint mechanisms that block transitions between cell-cycle phases when cells encounter stressful conditions. For example, DNA damage activates checkpoints that delay cell-cycle progression and trigger DNA repair. Under severe stress, DNA damage checkpoints may trigger permanent cellular outcomes such as apoptosis or senescence. Failure to fully activate DNA damage checkpoints can lead to genome instability, as the unrepaired DNA damage can be passed on to the next generation of cells

(Nyberg et al., 2002; Sogo et al., 2002). On the other hand, because cells routinely experience low levels of endogenous DNA damage (Vilenchik and Knudson, 2003), timely checkpoint recovery after DNA damage repair is necessary for continued cell proliferation (Bartek and Lukas, 2007). Therefore, the balance between cell-cycle arrest and recovery must be regulated to continue proliferation in the face of constant exposure to endogenous and exogenous DNA damage sources.

Activation of DNA damage checkpoints is often accompanied by cell-cycle arrest, which provides a temporal delay necessary to repair DNA lesions before resuming proliferation (Paulovich et al., 1997; Shaltiel et al., 2015; Wang et al., 2015). The precise timing of events during a DNA damage checkpoint response is not entirely clear. For example, it is not known how abrupt the pause is; whether the pause is a complete halt or a graded reduction in cell-cycle progression; or how the duration of the pause changes in response to different DNA damage doses or during different cell-cycle phases. Recent live-imaging studies in single cells have shed light on some of the underlying parameters that confer differential sensitivity to endogenous DNA damage. For example, cell-to-cell variation in p21 levels leads to differences in checkpoint stringency (i.e., the robustness of cell-cycle arrest in response to DNA damage) (Arora et al., 2017; Barr et al., 2017). However, the underlying parameters that result in differential responses within a cell-cycle phase and in response to exogenous DNA damage are generally unknown. Knowledge of these collective dynamical behaviors (which we refer to as DNA damage checkpoint dynamics) is necessary for understanding the relationship between the DNA damage response (DDR) and functional cellular outcomes such as permanent cell-cycle arrest.

Among the various forms of DNA damage, DNA double-strand breaks (DSBs) are one of the most harmful types of lesions (van Gent et al., 2001). DSBs can give rise to chromosome rearrangements and deletions that can subsequently lead to cancer. The functional effects of DSBs can vary depending on the cell-cycle phase in which the damage was incurred. For example, it has long been known that cells in different cell-cycle phases show drastic differences in survival under the same levels of ionizing radiation, which induces DSBs (Pawlik and Keyomarsi, 2004). The underlying basis for these differences in cell survival is not

clear. One explanation for the observed differences in survival among the cell-cycle phases is that each phase employs unique molecular mechanisms to enforce the checkpoint. Indeed, the concept of distinct DNA damage checkpoint mechanisms at different stages of the cell cycle, such as G1/S, intra-S, and G2/M, has long existed. Precisely how these checkpoint dynamics are executed throughout each cell-cycle phase, however, is not clear and requires real-time analysis of DNA damage checkpoint responses. Thus, a quantitative understanding of DNA damage checkpoint dynamics is crucial to linking the molecular pathways to predicted cell-cycle outcomes. This knowledge would not only help explain the difference in cell viabilities in response to DNA damage in different cell-cycle phases but would greatly inform efforts to predict clinical outcomes of genotoxic chemotherapies, which often target cells in a specific cell-cycle phase.

Here, we use fluorescence time-lapse microscopy to reveal the dynamics of DNA damage checkpoints for three major phases (G1, S, and G2) by monitoring cell-cycle progression upon acute DNA damage in otherwise unperturbed, asynchronously dividing single cells. In response to DSBs, each cell-cycle phase shows distinct DNA damage checkpoint dynamics. The G1 checkpoint employs a complete halt but is more permissive to DNA damage than the G2 checkpoint because it is temporally located well before the G1/S boundary. The S phase checkpoint is the least sensitive to DNA damage and does not completely halt cell-cycle progression, but rather continuously slows the rate of progression throughout the remaining duration of S phase. The most stringent checkpoint occurs during G2, which abruptly and completely halts cell-cycle progression by imposing a delay that is linearly correlated with the amount of DNA damage. Because of the internally located checkpoint in G1 and the graded slowdown of cell-cycle progression in S phase, both phases show a strong dependence between the timing of DNA damage within the phase and the functional outcome in response to DNA damage. Taken together, our results argue that the timing of DNA damage relative to cell-cycle phases determines the sensitivity, dynamics, and functional outcomes of checkpoint responses.

RESULTS

A Quantitative Model of DNA Damage Checkpoint Dynamics and Cell-Cycle Phase Transitions

DNA damage checkpoint regulation is a dynamic process that needs to adapt to changing environments. These checkpoints must balance the activation and the inactivation of arrest mechanisms in order to prevent lethal consequences of DNA DSBs, while allowing cell growth and proliferation. When damage occurs within a cell-cycle phase, checkpoint mechanisms halt cell-cycle progression until the damage is repaired before allowing transition to the next phase (Figure 1A). To gain a systematic understanding of DNA damage checkpoint dynamics, we developed a quantitative, cell-cycle phase-specific checkpoint model that was based directly on observed cell-cycle transitions in asynchronously proliferating cell populations. For asynchronously proliferating cells that experience DNA damage at different times during a given cell-cycle phase, DNA damage checkpoint dynamics can be visualized by a “transition curve”

that captures the rate of transition out of a specific cell-cycle phase. To be precise, a transition curve plots the cumulative percentage of cells that transition into the next cell-cycle phase against the post-damage transition time, the interval duration between the time of damage and the moment of transition into the next phase (Figure 1B). The plateau in each transition curve represents the time at which nearly all cells have successfully transitioned to the next phase. An advantage of this data-driven model-building approach is that it requires only three conservative assumptions. First, a cell exists in a single, discrete state (cell-cycle phase) at a given time (Elledge, 1996). Second, the transitions between states are complete and irreversible (Novak et al., 2007; Barr et al., 2016; Cappell et al., 2016). Third, DNA damage can affect the timing of these transitions through activation of checkpoint mechanisms (Branzei and Foiani, 2008).

Under this DNA damage checkpoint model, there are two parameters that may vary in response to DNA damage levels. First, the duration of the delay in cell-cycle progression can lengthen with increasing amounts of DNA damage. This would correspond to a rightward shift of the transition curve (Figure 1C). Second, when the damage is too excessive to be repaired, a cell may exit the cell cycle and enter permanent cell-cycle arrest. As increasing levels of DNA damage increase the number of cells entering permanent arrest, the transition curve plateau lowers (Figure 1D). Under this model, cells can cope with increasing amounts of damage either by lengthening the duration of a temporary arrest, increasing the probability of entering permanent arrest, or both. By analyzing an asynchronous population of cells, one can gain insight into the dependency of DNA damage checkpoint sensitivity on the precise time within a cell-cycle phase, since the damage is essentially randomly distributed along the time axis of each cell-cycle phase. For example, in the case of damage level-dependent delay, as in Figure 1C, the same amount of damage causes a fixed delay duration independent of the timing of damage within the cell-cycle phase (Figure 1E, left panel). When in a cell-cycle phase whose early part is more sensitive to damage, cells that are damaged during early phase are arrested for longer durations than cells damaged near the end of the phase, resulting in a less-steep transition curve (Figure 1E, middle panel). Similarly, a cell-cycle phase that is more sensitive toward the end of the phase shows steeper transition curves (Figure 1E, right panel).

Quantification of Cell-Cycle Progression in Individual, Asynchronously Proliferating Cells

To test whether cells employ a dose-dependent arrest duration or a dose-dependent permanent arrest, we developed a fluorescent reporter system that allows real-time monitoring of cell-cycle phase transitions in individual proliferating cells. Our goal was to quantify the duration of time a cell spends in G1, S, and G2-M. These three durations were quantified by recording four time points for each cell: the beginning of the cell cycle, the onset of S phase, the end of S phase, and the end of the cell cycle (Figure 2A). The beginning and end of each cell cycle was recorded as the time of telophase of the mother cell and the time of telophase of the given cell, respectively. These two measurements indicate the total cell-cycle duration for each cell. To determine the beginning and end of S phase, we developed a modified reporter for S phase progression by fusing the red fluorescent

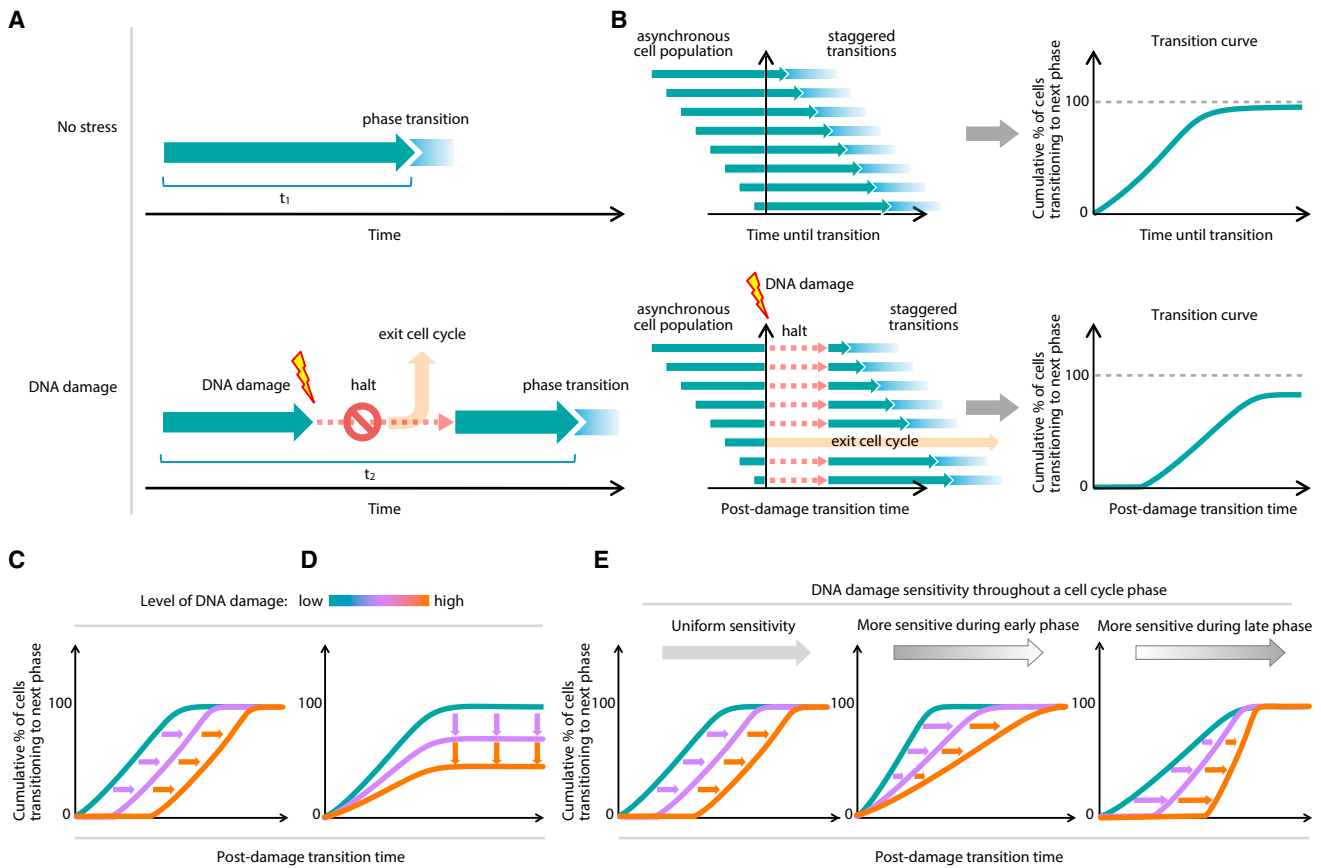


Figure 1. Model of DNA Damage Checkpoint Dynamics

(A) “Arrest-and-restart” model of cell-cycle checkpoint dynamics in response to DNA damage. The green arrow represents unrestricted progression of a cell-cycle phase through time. In the absence of DNA damage, cells progress readily through a phase with duration t_1 . When damage occurs, progression through a phase is temporarily interrupted, resulting in an increase in phase duration, t_2 .

(B) Schematic of a transition curve. A transition curve is obtained by measuring the post-damage transition times of an asynchronous population of cells that are damaged at different points during a particular cell-cycle phase. Each green arrow represents an individual cell’s progression through a particular cell-cycle phase. The transition curve plots the cumulative percentage of cells that have successfully transitioned to the next phase as a function of time.

(C) Transition curves expected from a graded halt duration response to DNA damage level. Increasing damage causes a corresponding delay before cells transition to the next cell-cycle phase.

(D) Transition curves expected from a graded permanent arrest response to DNA damage level. Increasing damage results in fewer cells transitioning to the next phase.

(E) Expected transition curves when DNA damage sensitivity varies throughout a cell-cycle phase. The intensity of gray arrows indicates the DNA damage sensitivity. Increased sensitivity during the early parts of a phase allows cells that are already near the end of the phase to transition more readily (middle plot). Greater sensitivity in the later part of a phase results in an immediate delay to transition of the population (right plot).

protein mCherry to the proliferating cell nuclear antigen (PCNA) (PCNA-mCherry; Figure 2B). Multiple studies have shown that PCNA exhibits distinct punctate localization patterns at specific times within S phase (e.g., sub-phases), and PCNA returns to diffuse nuclear localization upon exit from S phase (Kisielewska et al., 2005; Pomerening et al., 2008; Burgess et al., 2012; Zeratke et al., 2017).

To investigate both functional DNA damage checkpoint dynamics and to understand how disrupted checkpoints can lead to distinct dynamics, as is often found in cancer cells, we stably expressed the PCNA-mCherry reporter in both retinal pigmented epithelial (RPE-1 hTERT, abbreviated RPE) cells and in the osteosarcoma cell line U2OS. RPE cells are non-transformed human epithelial cells immortalized with telomerase reverse transcrip-

tase with intact checkpoints, whereas U2OS cells are a transformed cancer cell line which has an attenuated p53 response and an unstable G1 checkpoint due to the expression of truncated Wip1 and a p16 deficiency, both of which are important for overriding the G1 checkpoint (Diller et al., 1990; Stott et al., 1998; Akan et al., 2012; Kleiblova et al., 2013). We imaged freely proliferating cells through multiple cell divisions without affecting the cell-cycle distribution properties (Figure S1A) or the cell-cycle length (Figure S1B) as measured through flow cytometry and a traditional cell counting approach, respectively. These controls indicate that time-lapse imaging did not significantly alter cell-cycle progression. As expected, we found that PCNA-mCherry formed replicative foci that appeared abruptly at the onset of S phase and disappeared abruptly at the end of

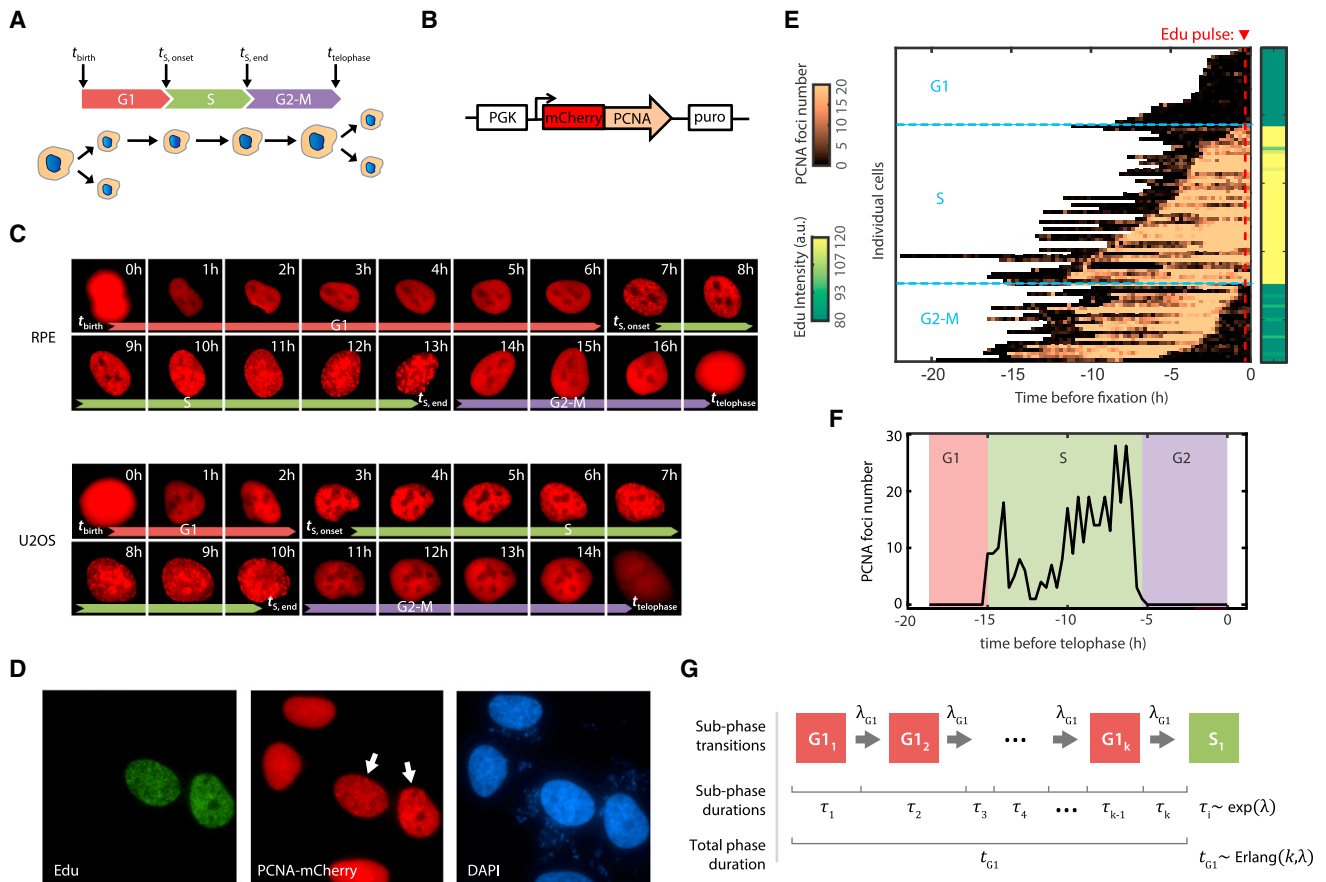


Figure 2. Measuring and Modeling Cell-Cycle Phase Progression in Single Cells

(A) Cell-cycle diagram showing three phases (G1, S, and G2-M) defined by four measured time points.

(B) Schematic showing the construct design for PCNA-mCherry reporter.

(C) Sequence of live-cell images of RPE and U2OS cells expressing the PCNA-mCherry reporter.

(D) Immunofluorescence (IF) staining for Edu incorporation in the reporter cell line. U2OS cells expressing PCNA-mCherry were pulsed with 10 μM Edu for 1 hr, fixed, and stained for Edu and DAPI. White arrows indicate S phase cells with punctate PCNA pattern.

(E) Live-cell imaging combined with fixed-cell IF staining with Edu incorporation. Asynchronously cycling U2OS cells expressing the PCNA-mCherry reporter were imaged for 24 hr, and the number of PCNA foci in each cell was quantified every 15 min. At the end of the movie, cells were pulsed with 10 μM Edu for 15 min, fixed, and quantified for Edu incorporation.

(F) Method for S phase identification based on PCNA-mCherry foci trajectories. The plot shows a typical single-cell time series of PCNA foci number. The onset and the end of S phases were identified by the initial maximal increase and final maximal drop, respectively, in the number of PCNA foci.

(G) Schematic of computational model for cell-cycle progression. G1, S, and G2-M phases were each modeled as a series of k identically distributed sub-phases with exponential waiting times of rate λ . Thus, the total duration of each phase followed an Erlang distribution with shape parameter k and scale parameter $1/\lambda$. DNA damage was modeled either by interrupting or slowing the rate of sub-phase progression (see [Method details](#)).

S phase during the transition to G2 (Figure 2C). The emergence of PCNA-mCherry foci correlated strongly with Edu incorporation, while cells in other phases showed diffuse nuclear fluorescence (Figures 2D and 2E). This pattern of foci accumulation reliably identified the beginning and end of S phase with 15-min precision (Figures 2E and 2F). Thus, we established a system that quantifies, for individual cells, the duration of time spent in G1, S, G2-M, and, thus, the entire cell cycle.

Computational Model of Cell-Cycle Progression

We then developed a computational model to stochastically simulate cell-cycle progression of RPE and U2OS cells with the goal of eventually understanding how DNA damage affects the rate of progression. We model each cell-cycle phase inde-

pendently as a series of steps, with total number of k steps, and a progression rate (λ) through each step (Figure 2G, see [STAR Methods](#) for details). Therefore, each step of a cell-cycle phase can be described as a Poisson process, and the total cell-cycle phase duration can be modeled as an Erlang distribution (Soltani et al., 2016). Because the model is characterized by a sequence of steps with the same rate, it is straightforward to introduce rate changes into cell-cycle progression. By fitting the experimentally measured distributions of cell-cycle phase durations, we obtained two parameters for each phase: shape (k) (which can be interpreted as the number of steps within a cell-cycle phase) and scale ($1/\lambda$) (which can be interpreted as the average timescale for each of the steps) (Figures S1C and S1D, upper panels). Using the estimated parameters, we

were able to accurately simulate the cell-cycle phase transitions under basal conditions in an asynchronous population with phase durations drawn from the fitted Erlang distribution (Figures S1C and S1D, lower panels).

Each Cell-Cycle Phase Displays Distinct DNA Damage Checkpoint Dynamics

With this reporter system and computational model in place, we experimentally determined DNA damage checkpoint dynamics for each cell-cycle phase in individual RPE and U2OS cells. We induced DSBs in asynchronously dividing cells using the radiomimetic drug neocarzinostatin (NCS) and recorded the cell-cycle phase in which the damage occurred. Confirming that NCS induced similar numbers of DSBs in each cell-cycle phase (Figure S2A) without affecting the PCNA-mCherry reporter's accuracy (Figures S1E and S1F), we then followed each treated cell and measured the time until that cell exited its current cell-cycle phase and transitioned to the next cell-cycle phase. This analysis produced a transition curve for each dose of NCS and cell-cycle phase (Figures 3A and 3B, solid lines). With no external stress, nearly all of the RPE and U2OS cells transitioned to the next phase (>99%). As the dose of NCS was increased, however, two effects were observed. First, for cells damaged in G1 or G2-M, increasing NCS concentrations reduced the number of cells that completed transitions within the 48-hr observation window, indicating a dose-dependent increase in the permanent arrest probability. Secondly, high DNA damage doses increased the time delay before half of the phase transitions occurred, particularly for cells damaged in G2-M, indicating a dose-dependent increase in delay duration.

Several additional interesting observations emerged from these transition curves. In both RPE cells, which had a functional G1 checkpoint, and U2OS cells, which have an unstable G1 checkpoint (Diller et al., 1990; Stott et al., 1998), the G1 transition curves exhibited a hyperbolic shape without an immediate delay (Figures 3A and 3B). In contrast, cells damaged during S phase transitioned to G2 without interruption for all but the highest NCS levels, indicating a low sensitivity of the S phase checkpoint to DSBs. The few S phase transition curves that did show a response to NCS also demonstrated a hyperbolic shape similar to the G1 cells. In addition, almost all RPE and U2OS cells (>99%) damaged during S phase with the highest NCS concentrations were permanently arrested in the subsequent G2-M phase. We observed comparable or even higher arrest probabilities of G2-M arrest after S phase damage than in cells damaged during G2-M with lower NCS concentrations (Figures S2C–S2H). This pattern suggested that cells relied on the checkpoint in G2-M to prevent catastrophic consequences of DNA damage incurred during S phase. In sharp contrast, cells damaged in G2 or M showed a sigmoidal transition curve with an immediate delay. Although the molecular pathways of the DDR in each cell-cycle phase employ redundant mechanisms (Shaltiel et al., 2015), these results imply that each phase employs distinct DNA checkpoint dynamics. In addition, we found that the transition curves exhibited qualitatively similar features in response to zeocin, a member of the bleomycin antibiotics that induces DNA damage (Figures S2I–S2K), suggesting that the checkpoint responses were general to DNA damage but not specific to a particular DNA damaging agent.

To explain these complex dynamics within our model framework, we fit our experimental data with the “arrest-and-restart” checkpoint model presented in Figure 1A. The model has two adjustable parameters: the duration of the cell-cycle halt, and the percentage of cell entering permanent arrest (Figures S3A–S3F, dashed lines; Table S1 for fitted parameters, see the STAR Methods for details). In brief, the halts were modeled by introducing additional times to the cell-cycle phase; the permanent arrest fractions were incorporated by randomly selecting a fraction of cells to exit the cell cycle. Although the model reproduced some features of the transition curves, there were significant discrepancies between the model fits and the data, suggesting that important features of the DNA damage checkpoints were not captured by the “arrest-and-restart” checkpoint model outlined in Figure 1A. For example, cells damaged in G1 transitioned to S phase at the same rate as unstressed cells until ~3 hr after damage, at which point the transition curve began to flatten. This initial rise in transition curves was also observed in G2-M for the first ~1 hr after damage. This behavior could be explained by a checkpoint commitment point that was temporally located roughly 3 hr (G1) or approximately 1 hr (G2-M) before the end of the phase. Cells that have passed such a DNA damage “commitment point” are already irreversibly committed to transitioning at the time of damage despite experiencing DNA damage. A second feature of the data that was not well captured by the model was the hyperbolic shape of the curves observed in S phase, which often showed gradual rightward shifts at the 50% transition point. These features could be explained by a slowing down (rather than a complete halt) of cell-cycle progression when the checkpoint was activated by DNA damage.

A Refined Model of DNA Damage Checkpoint Regulation of Cell-Cycle Progression

In gap phases, DNA damage checkpoints prevent cells with significant DNA damage from entering the next cell-cycle phase. The simplest description of these checkpoints is that they block transition to the next phase regardless of when the damage occurs within the phase (Figure 1A). However, the observed transition curves prompted us to consider the possibility of a “commitment point” located at some internal point of a cell-cycle phase after which DNA damage does not prevent a successful transition. The exact temporal location of such a commitment point is unclear. For example, a commitment point could exist at the phase-phase boundaries, resulting in arrest essentially regardless of when the damage occurs (Figure 3C, upper plot). Alternatively, the commitment point may be located somewhere internal to the cell-cycle phase (Figure 3C). In the latter case, once a cell passes this point, it would not be subject to arrest by a DNA damage checkpoint in that phase but would presumably affect progression through the next phase. This model would be expected to lead to a delay in the divergence of the transition curves at all DNA damage doses (Figure 3D). Moreover, we also allow that the cellular consequence of the checkpoint activation may not lead to a complete halt of cell-cycle progression, which we refer to as “all-or-none” checkpoint activation (Figure 3E, upper axis). Instead, the checkpoint enforcement could induce a partial slowdown of cell-cycle progression that adjusts the *rate* of progression relative to the extent of DNA damage level. We refer to

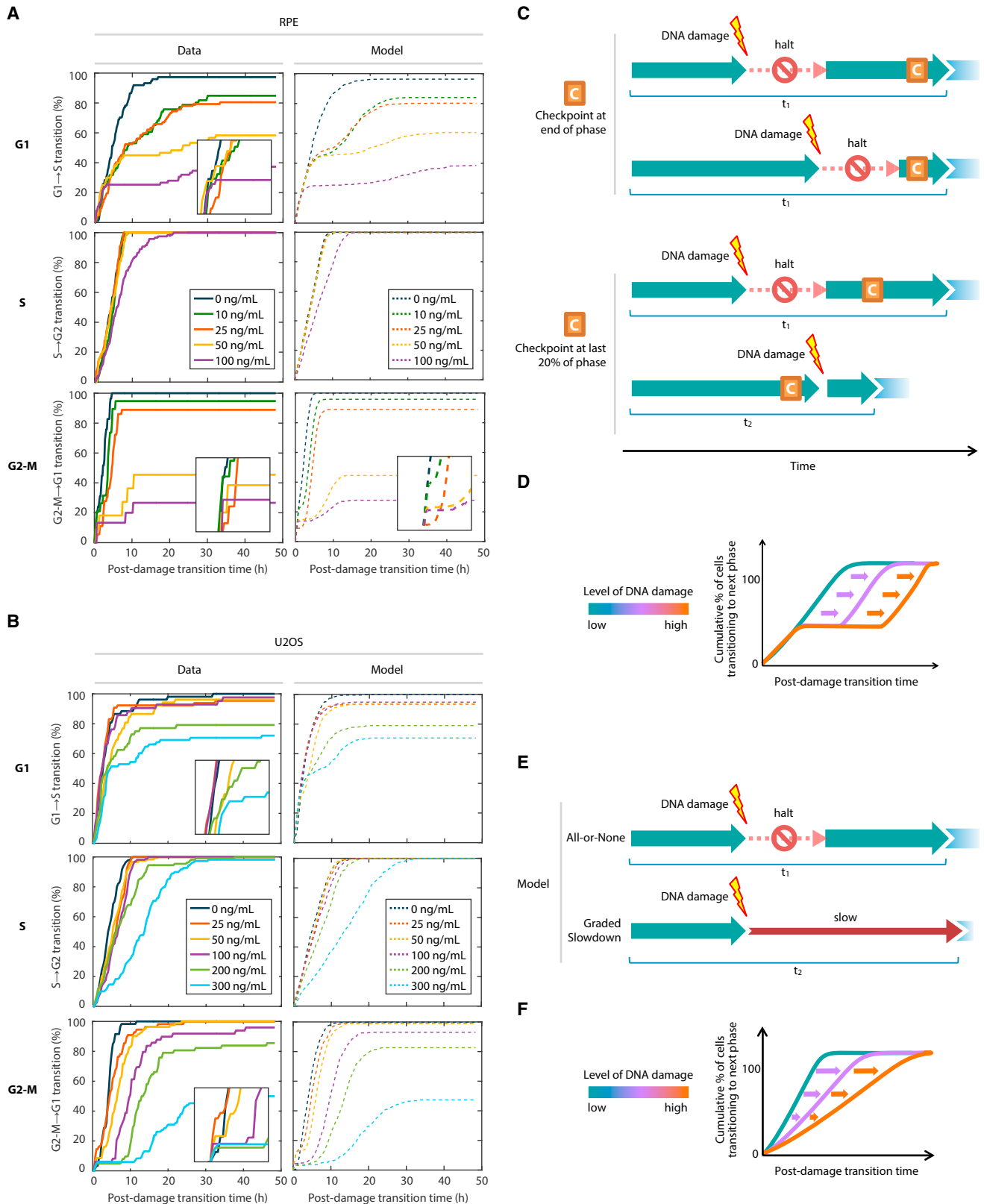


Figure 3. Each Cell-Cycle Phase Exhibits Distinct DNA Damage Checkpoint Dynamics

(A and B) Cell-cycle phase-specific transition curves in response to acute DNA damage in (A) RPE or (B) U2OS cells. Left panels and solid lines: transition curves for asynchronously dividing cells treated with NCS at the indicated concentrations during G1, S, or G2-M. For each cell, we quantified the time interval between (legend continued on next page)

this model of checkpoint enforcement as having “graded slowdown” kinetics (Figure 3E, lower axis). Graded slowdown checkpoint kinetics would lead to a decreased slope in the transition curves (Figure 3F).

To distinguish among these possibilities, we sought evidence of an internally located commitment point as well as checkpoint enforcement through graded slowdown kinetics. Computational simulations revealed a qualitative difference in the transition dynamics under different DNA damage checkpoint models (Figures S3G–S3J, see Method Details). For checkpoints (e.g., G2-M) that triggered an abrupt and complete halt, the transition curves exhibited a sigmoidal shape with an immediate delay in transition right after damage (Figure S3G). In contrast, under the graded slowdown model, where cells partially slowed down their progression in response to DNA damage, the transition curves were hyperbolic (Figure S3H), as seen mostly in S phase and occasionally in G1. Furthermore, simulations that incorporated the internal checkpoint location revealed a delay in divergence of the curves under both checkpoint models (Figures S3I and S3J, compare red line to other lines) as seen, for example, in the G1→S transition for both RPE and U2OS cells (Figures 3A and 3B).

We then fit each phase of our experimental data to the refined model of two different kinetics (all-or-none and graded slowdown) and determined the kinetics that gave a better fit (Figures 3A and 3B, dashed lines, S4A and S4B; Tables S2 and S3, see Method Details). For G1 in RPE and G2-M in both cell types, the data were consistent with all-or-none checkpoint kinetics. In addition, both G1 and G2-M showed evidence of internally located commitment points in both cell types. We estimated the commitment point location to be ~60% (average among individual estimates from non-zero NCS concentrations, 51%–75%) of the full G1 duration for RPE and ~50% (35%–68%) for U2OS cells. For the combined G2-M phases, we detected commitment points at ~80% (76%–90%) and ~90% (85%–96%) of the full G2-M duration for RPE and U2OS, respectively (Tables S2 and S3). Since entry into M phase is known to temporarily silence the DDR (Heijink et al., 2013; Orthwein et al., 2014), this temporal position likely corresponds to the G2/M boundary, which was not precisely resolved in our system. For S phase cells, however, the graded slowdown checkpoint kinetics produced a better fit for both RPE and U2OS, with the commitment point located at 97% (96%–97%) and 96% (90%–100%) of S phase, respectively. Overall, the G1 commitment point estimates showed the highest

variability among different NCS concentrations, which could be due to the heterogeneity in G1 durations (Figures S1C and S1D). However, commitment point estimates were in agreement within G1 but significantly different from those of G2. In addition, when we repeated the fitting, the estimates under the highest NCS concentrations fell into a defined distribution (Figures S4C–S4F). Altogether, our results suggested that cells in G1 and G2-M implemented an all-or-none checkpoint activation, whereas checkpoint responses in S phase showed graded slowdown kinetics. Furthermore, the G1 commitment point was located well before the G1/S boundary. In addition, the refined model predicted that both the halt duration and the permanent arrest probability in gap phases increase with the level of DNA damage (Figures S5A–S5D). However, cells damaged in G1 and G2-M that transitioned into the next phase were significantly affected in the subsequent gap phase, either by prolonging the phase or by increasing the permanent arrest probability (Figures S5E–S5L). These results further suggest that the commitment points in G1 and G2-M both represent a “point-of-no-return” regardless of the levels of DNA damage.

G1 and G2 Checkpoints Completely Halt Cell-Cycle Progression

We next sought to verify the predictions of our refined DNA damage checkpoint model. Specifically, the model predicts a dose-dependent halt duration in phases that display all-or-none checkpoint activation such as G1 or G2-M. It also predicts that these checkpoints are enforced at internally located commitment points. This would presumably lead to two populations of cells depending on the timing of DNA damage: cells damaged before the commitment point should be equally delayed in phase progression regardless of when the damage occurs, whereas cells damaged after the commitment point should proceed to the next phase without delay. In contrast, the model predicts that cells damaged in S phase should partially delay their transition to G2 in proportion to the amount of damage. We examined the distributions of post-damage transition times in the three cell-cycle phases, which showed evidence for two distinct checkpoint kinetics (Figure 4). Indeed, in the phases where our models predicted an all-or-none checkpoint (G1 or G2), we also observed distinct gaps in post-damage transition times (Figures 4A and 4C). The gap was most dramatic in G2-M, suggesting a checkpoint that imposed a stringent time delay in response to DNA damage; all cells that had not passed the

NCS treatment and the transition from its current cell-cycle phase to the next phase. Right panels and dashed lines: best fit lines of the experimental data to the refined DNA damage checkpoint model that incorporated both the flexible checkpoint location and the possibility of graded slowdown checkpoint kinetics (S phase) described in Figures 3C–3F. RPE G1: n = 74, 66, 82, 60, and 75; S: n = 139, 97, 98, 69, and 118; G2-M: n = 29, 19, 36, 11, and 15 (order corresponds to 0, 10, 25, 50, and 100 ng/mL). U2OS G1: n = 52, 65, 52, 42, 48, and 68; S: n = 140, 120, 119, 160, 109, and 109; G2-M: n = 59, 55, 81, 49, 62, and 84 (order corresponds to 0, 25, 50, 100, 200, and 300 ng/mL).

(C) Schematic of models for variable DNA damage checkpoint location. The model incorporates a temporally located commitment point. Upper plot: end of phase, where the commitment point is located at the end of the phase (i.e., 100% of the way through). Lower plot: last 20%, where the commitment point is located at 80% of the way through the phase. Cells that are damaged after this time point transition to the next phase without arrest.

(D) Expected transition curves under the model of a DNA damage checkpoint that is internally located. The initial increase in transition percentage for all damage levels represents the fraction of cells that were beyond the commitment point.

(E) Schematic of models for DNA damage checkpoints with different kinetics. Upper plot: a checkpoint that is enforced in an all-or-none manner halts the cell-cycle progression completely upon DNA damage. Lower plot: a checkpoint that is enforced by slowing down the rate of cell-cycle progression upon DNA damage without completely halting the progression.

(F) Expected transition curves under the graded slowdown kinetic checkpoint model. The change in slopes among different DNA damage levels results from differences in the time of damage for individual cells. Cells damaged earlier in the phase experience a longer delay.

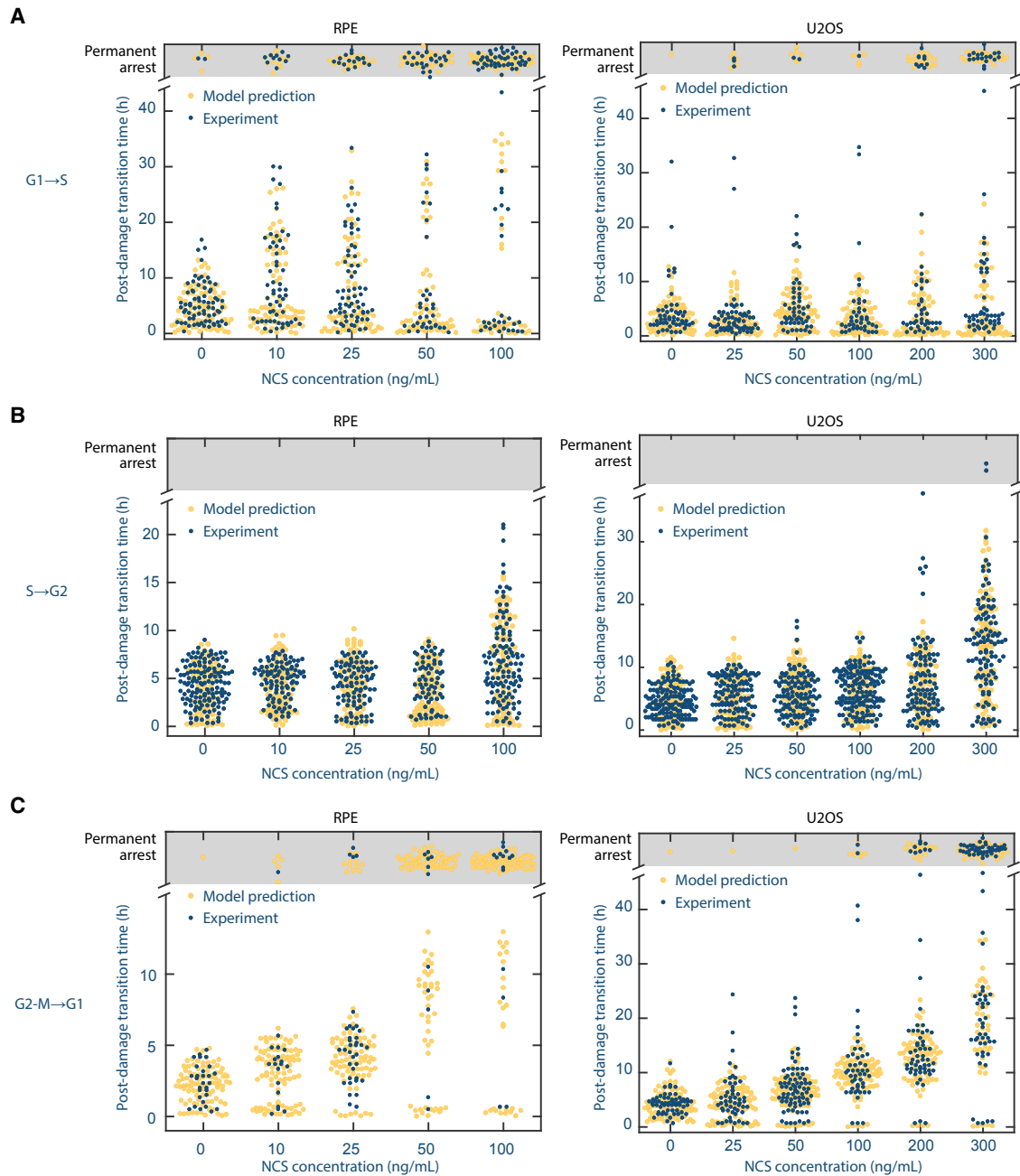


Figure 4. The G1 and G2 DNA Damage Checkpoints Enforce a Complete Halt to Cell-Cycle Progression by an Interval that Is Proportional to the Damage Level

(A) The post-damage G1 → S transition time durations of cells damaged anytime during G1 in RPE (left) and U2OS (right) cells.

(B) The post-damage S → G2 transition time durations of cells damaged anytime during S in RPE (left) and U2OS (right) cells.

(C) The post-damage G2-M → G1 transition time durations of cells damaged anytime during G2 or M in RPE (left) and U2OS (right) cells.

commitment point were arrested for a substantial time. In contrast, cells damaged during S phase showed continuous distributions of post-damage transition times without any obvious gaps, consistent with the model's prediction of graded slowdown checkpoint dynamics (Figure 4B). We thus concluded that our refined model captured many of the DDR dynamics displayed by proliferating cells.

We next characterized the checkpoint kinetics with respect to the arrest durations. Because the G2-M checkpoint provided the strongest evidence of a stringent, complete halt with a late and consistent commitment point, we focused our studies on the G2-M arrest kinetics.

The model predicted that the commitment point locations for G2-M were relatively close to the end of the combined G2-M

phase (80% for RPE and 90% for U2OS). Consistent with the model prediction, we noticed only a small population (19% for RPE; 6% for U2OS) of G2-M cells that escaped the checkpoint and divided immediately after the highest two levels of NCS treatment (Figure 4C). These sub-populations that divided soon after DNA damage likely represent cells that had already entered mitosis, since the entry into mitosis has been shown to temporarily inactivate the DDR (Heijink et al., 2013; Orthwein et al., 2014; Shaltiel et al., 2015). Indeed, based on the average G2-M durations for RPE (3.9 hr) and U2OS (6.5 hr) (Figures S1C and S1D), the model predicted the checkpoint location to be ~0.7–0.8 hr before division. Since the average M phase lasted approximately 40 min under basal conditions based on nuclear envelope breakdown revealed by differential interference contrast images (Figures S5M–S5O), the predicted commitment point location coincided with the G2/M boundary. Although the duration of mitosis in U2OS cells appeared to increase under the highest NCS concentrations (Figure S5O), this does not affect the estimation of the commitment point location because that estimation relies on immediately transitioning cells that do not show arrest or delay. Because the DNA damage checkpoint response was presumably activated before reaching the G2/M boundary, we infer that the checkpoint delays observed in our data were enforced entirely within G2 and not M phase. We therefore refer to this checkpoint as simply the G2 checkpoint henceforth.

The G2 checkpoint may impose a constant time delay upon a threshold level of DNA damage, or it may be programmed to calibrate the delay durations according to DNA damage levels, as suggested by the model fitting (Figures S5A and S5B). To distinguish between these possibilities, we examined the time gap between the onset of acute DNA damage and the next transition time point. We found the time delay to be prolonged with increasing NCS concentration (Figure 4C), in linear proportion to the level of DSB incurred (Figures S5P and S5Q). Furthermore, the arrest durations were independent of when the cells were damaged within G2 (Figures S5R and S5S). Together, these results suggested that the majority of G2 phase was under the protection of the DNA damage checkpoint. In response to acute DNA damage, the G2 checkpoint abruptly imposed a time delay that was proportional to the level of damage and independent of the progression stage of G2 phase.

The Graded Slowdown and Non-terminal Commitment Point Location Link Cell-Cycle Outcome to Cell-Cycle Stage

Our findings thus far indicate that each cell-cycle phase has distinct DNA damage checkpoint kinetics and commitment locations. Although the two mechanisms are distinct, both the internal checkpoint location and the graded slowdown models predict that an individual cell's transition kinetics depend on the precise time that the cell experiences DNA damage. In the case of an internally located commitment point, DNA damage leads to arrest only when it occurs before the commitment point. In the case of a graded slowdown mechanism, cells that experience damage earlier during a phase would be expected to take longer to complete that phase since there is more remaining time subjected to the slowdown. We sought to test these predictions with further analyses of cells damaged at different times during

each phase. We used asynchronously dividing cells damaged at different points during G1, S, and G2-M phases and plotted the total phase duration against the time already spent in that phase (Figure 5A).

To investigate the functional outcomes of these checkpoint responses, we categorized cells into three groups: unaffected (cells with total duration not significantly different from the control distribution), temporary arrest (cells with prolonged cell-cycle phase but eventually transitioned by the end of the 48-hr experiment, which can be due to either all-or-none or graded slowdown checkpoint kinetics), and permanent arrest (cells that did not transition within 48 hr) (Figures 5B, S6A, and S6B). Although transitions could potentially occur after 48 hr, most transitions took place during the first 35 hr, with a small number of additional transitions afterward (Figure 4), indicating statistically different responses between the transitioned and un-transitioned groups.

To assess cell-cycle outcomes from DNA damage in different cell-cycle phases, we plotted the three categories of cell-cycle outcomes as a dose response for each cell-cycle phase (Figures 5C–5E and S6C–S6H). Several interesting features emerged from this analysis. First, in all three phases, a smaller fraction of U2OS cells were affected by the same NCS concentrations compared with RPE, indicating a higher tolerance to DSBs as expected. Second, S phase cells had the highest NCS tolerance and responded only by temporary slowdown (Figure 5D), but presumably underwent permanent arrest in the subsequent G2 (Figures S2C–S2H). Third, in both G1 and G2, cells preferred temporary arrest response to low NCS levels, but changed to permanent arrest in response to high NCS. Unlike during G1, when temporary arrest was never a predominant outcome (always <40%) and the change from temporary to permanent arrest was gradual (Figure 5C), G2 cells preferred temporary arrest in response to low NCS, but displayed a sharp switch to permanent arrest at around 40 ng/mL NCS in RPE and around 300 ng/mL in U2OS. The total fraction of affected cells (cells undergoing temporary or permanent arrest) was higher in G2 compared with G1 in both RPE and U2OS. Thus, the G2 checkpoint is overall the most stringent checkpoint, because fewer damaged cells escaped the checkpoint response. In sum, the results suggested G1 and S phase checkpoints involve a gradual transition to permanent and temporary arrests, respectively, whereas the G2 checkpoint includes a sharp threshold above which cells switch to permanent arrest.

Finally, we asked whether cell-cycle outcome depended on the timing of DNA damage within a cell-cycle phase. Simulations revealed that, under the all-or-none model, the affected fraction was independent of cell-cycle phase stage at the time of damage, as long as the damage occurred before the commitment point (Figures 6A and S7A, middle panels). In contrast, under the graded slowdown checkpoint model, the fraction of cells affected was inversely proportional to the progress into that phase at the time of damage (Figures 6A and S7A, right panels). Consistent with the model prediction, the total S phase durations were linearly and inversely correlated with the time spent in S phase before damage, with a slope consistent with the model-predicted slowdown factors (Figures 6B and S7B–S7D). This relationship was in contrast to the all-or-none checkpoint kinetics in G2-M, where the total phase duration was independent

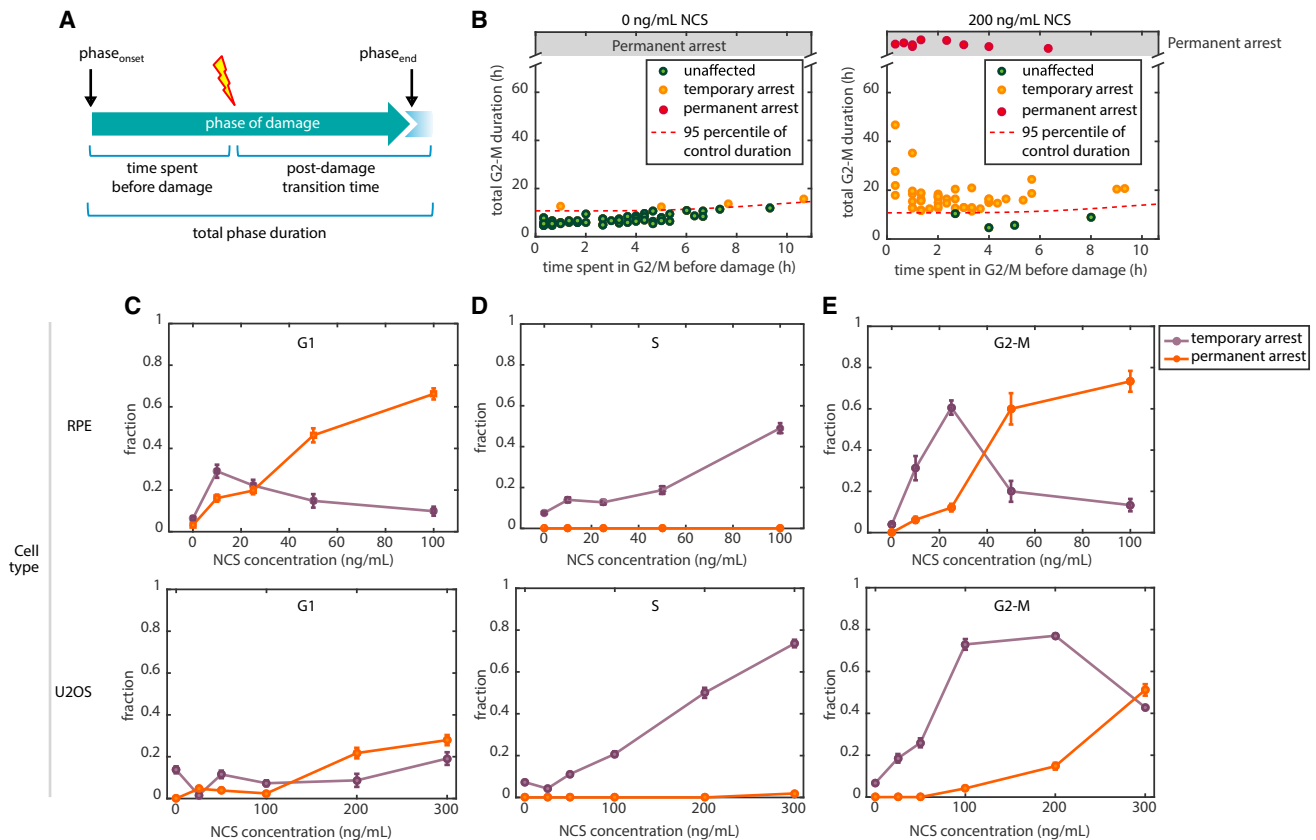


Figure 5. Cell-Cycle Outcomes as a Function of Cell-Cycle Phase at the Time of DNA Damage

(A) Schematic showing the definitions of time spent before damage, post-damage transition time, and total phase duration.

(B) Classifying individual cells into three cell-cycle outcomes based on phase duration. Here, we show U2OS cells treated during G2-M to demonstrate the classification strategy. Untreated cells (left) were used to identify a subpopulation of cells whose phase durations fell above the 95% percentile. These cells were considered to be arrested. Right: U2OS cells treated with 100 ng/mL NCS during G2-M showing a large fraction of cells above the threshold identified in the control population.

(C–E) Phase-specific cell-cycle outcomes in response to increasing doses of NCS treatment. Error bars represent binomial SE. Upper panels: RPE. Lower panels: U2OS.

of the timing of damage (Figures S5R and S5S). This correlation also argued against the possibility that the decreased slope in S phase transition curves was due to the increased variations in halt duration with increased DNA damage level.

When we examined the cell-cycle outcome's dependency on three stages within a given cell-cycle phase at time of damage (early, middle, and late), we noted consistent patterns: Cells damaged earlier during a phase were more likely to be affected than cells damaged later (Figures 6C and S7E). The S phase checkpoint, which utilizes a graded slowdown checkpoint model, showed a linear decreasing effect as a function of time at the highest NCS concentration in RPE (Figure 6C, middle panel). In contrast, G2-M's early and middle stages, which presumably included only G2 cells, did not show a difference in arrest fraction, which was consistent with the abrupt all-or-none model (Figure 6C, right panel). The decreased fraction in the late stage was mostly due to the insensitivity to DSBs during mitosis. Therefore, this biphasic response in G2-M was characteristic of an all-or-none checkpoint model with a late commitment point. Furthermore, G1 checkpoint outcome was inversely dependent on the stage progression (Figure 6C, left panel),

consistent with a commitment point substantially earlier than the G1/S boundary.

DISCUSSION

Here, we used time-lapse fluorescence microscopy to study the dynamics of DNA damage checkpoints in asynchronously proliferating single human cells. We used single-cell data to build a phenomenological model of cell-cycle progression that incorporates the time-dependent effects of DNA damage. Our analysis reveals new aspects of cell-cycle phase-specific DNA damage checkpoint dynamics (Figure 7). Individual phases varied in several features: kinetics of the arrest response, the temporal location of an internally located commitment point, and the types of functional responses (e.g., temporary versus permanent arrest). These results provide a systematic characterization of DNA damage checkpoint dynamics that enhances our current understanding of cell-cycle checkpoint kinetics.

The different checkpoint kinetics predicted by our model can be explained by the underlying biological mechanisms of each checkpoint. The transition from G1 to S phase is marked by

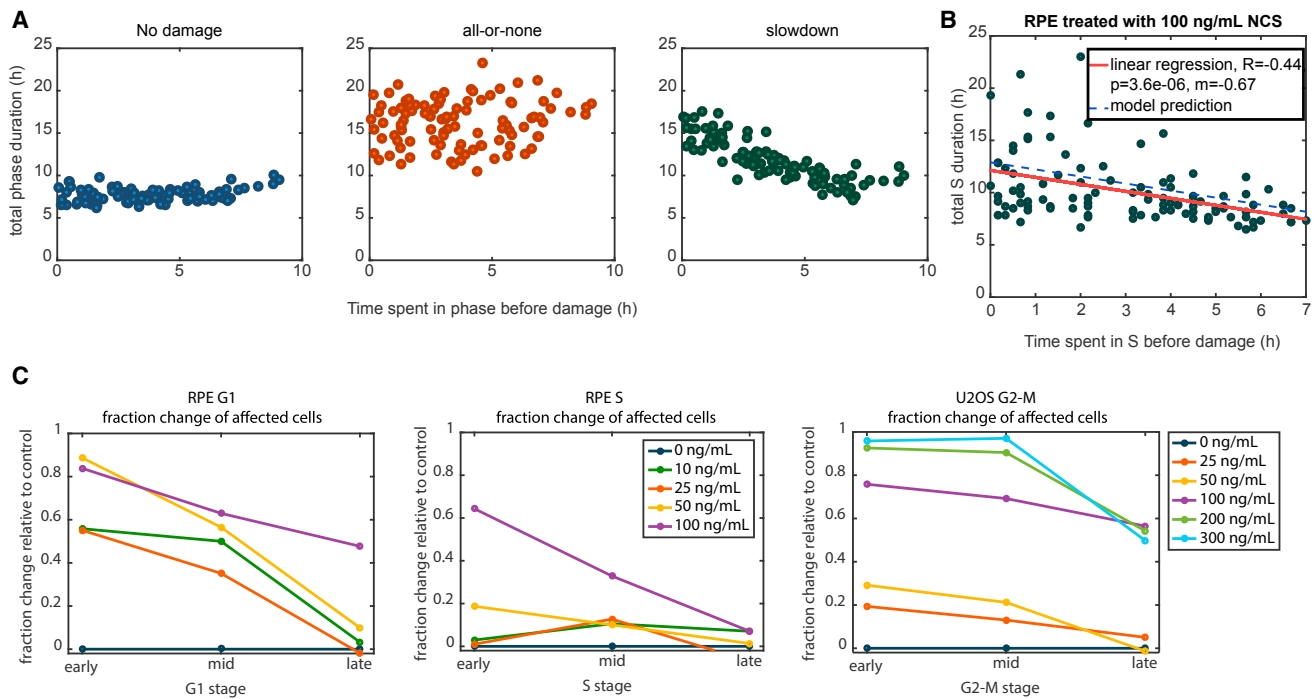


Figure 6. Cell-Cycle Outcomes Depend on the Timing of DNA Damage Both within and between Cell-Cycle Phases

(A) Simulations of cell-cycle phase durations as a function of time spent in that phase before damage. Simulations were performed using the fitted parameters (the shape, k , and scale, $1/\lambda$) from RPE's G1 phase distributions without taking into account the commitment point. In the cases with all-or-none checkpoint kinetics, the delay duration was 8 hr. In the cases with graded slowdown checkpoint kinetics, the slowdown factor was 0.5.

(B) The delay in S phase completion linearly depends on the timing of DNA damage within S phase. Experimental data of the total S phase durations as a function of time spent in S phase before damage in RPE cells under 100 ng/mL NCS. Red line represents linear regression of the experimental data. Blue dash line represents the model predictions of the mean S phase durations based on the graded slowdown checkpoint kinetics. The model parameters were based on the RPE's average S phase duration of 7.7 hr under basal condition and estimated slowdown factor of 0.60 under 100 ng/mL NCS.

(C) Dependency of cell-cycle outcome on the stage of cell-cycle phase progression. Representative cell-cycle outcomes for each phase's checkpoint are plotted as a function of cell-cycle phase stage: early, mid, or late stages. Fraction change relative to control was obtained by calculating the difference between the fraction of cells being affected (either temporary or permanent arrest) under NCS treatment and that without NCS treatment. G1 and S phases are shown for RPE cells, which display more physiological checkpoint responses than U2OS cells. G2 phase is shown for U2OS cells because the RPE G2 duration was too short to be readily subdivided into three stages. Cells were assigned to early, mid, or late stages based on whether the time they spent in that phase fell within the first, second, or third equal partition (tercile) of the theoretical distributions of time spent in each phase, respectively.

the activation of DNA synthesis from multiple origins of DNA replication, an event that requires active cyclin E/CDK2 and/or cyclin A/CDK2 (Labib, 2010; Tanaka and Araki, 2013). The transition from G2 to M phase requires a large increase in cyclin B/CDK1 activity (Taylor and Stark, 2001; Lindqvist et al., 2009). The all-or-none checkpoints we documented in both G1 in and G2 are consistent with switch-like mechanisms that inhibit the intracellular pools of cyclin/CDK complexes below their respective thresholds necessary for cell-cycle transitions. These mechanisms involve molecular entities such as the CDK inhibitor p21 and Wee1-mediated CDK inactivation (Donzelli and Draetta, 2003; Reinhardt and Yaffe, 2009). Without the corresponding cyclin-CDK complex activities essential to initiating DNA replication or mitosis, cell-cycle progression through the G1/S and S/G2 transitions is blocked rather than simply slowed.

In contrast, the graded slowdown kinetics we documented in S phase is consistent with the intra-S checkpoint mediated inhibition of late-origin firing. Complete genome duplication is normally achieved by establishing replication forks at thousands of individual DNA replication origins, but some origins fire at

the beginning of S phase, whereas others fire later. When DNA damage is detected (typically by stalled replication forks), nearby "dormant" origins that have not yet fired initiate replication to promote replication completion in that local region. At the same time, checkpoint pathways block new origin firing in other regions of the genome corresponding to late-replicating domains (Ge and Blow, 2010; Yekezare et al., 2013). Thus, DNA synthesis continues at forks emanating from the early-fired origins, but the overall rate of S phase progression is slowed (Paulovich and Hartwell, 1995; Tercero and Diffley, 2001). We postulate that this graded checkpoint response is protective to reduce the number of stalled replication forks that could collapse, snowballing the DNA damage (Cortez, 2015). Therefore, S phase actively counteracts the all-or-none mechanisms to avoid a prolonged stall with partially replicated DNA, a situation that could lead to disastrous genome instability.

The location of the proposed commitment point can affect the apparent checkpoint stringency in a particular cell-cycle phase. While both G1 and G2 utilize all-or-none checkpoint kinetics, the G2 checkpoint is more stringent than G1 in the sense that the

Cell cycle phase	G1	S	G2
Commitment point location			
Checkpoint kinetics	All-or-none	Graded slowdown	All-or-none
Halt duration	Increases with damage level	Not present	Increases with damage level
Sensitivity	Sensitive	Insensitive	Very sensitive
Cell cycle arrest mechanism	Gradual switch from temporary to permanent arrest with increasing damage level	Always temporary arrest	Sudden switch from temporary to permanent arrest with increasing damage level
Cell fate after transition	Arrest in subsequent G2	Arrest in subsequent G2	Arrest in subsequent G1

Figure 7. Summary of Checkpoint Dynamics as a Function of Cell-Cycle Phase in RPE Cells

commitment point occurs very close (within 0.5 hr) to the G2/M border. This temporal location of the G2 commitment point is consistent with previous observations and may be concurrent with the onset of antephase described previously using time-lapse analysis (Xu et al., 2010; Krenning et al., 2014; Müllers et al., 2014, 2017; Feringa et al., 2016). In contrast, the G1 commitment point is located ~3–4 hr before the G1/S border in both RPE and U2OS, meaning that DNA damage within the last 3 hr of G1 usually fails to delay S phase onset. The earlier commitment point in G1 is consistent with previous observations that the G1 checkpoint fails to prevent S phase entry at early times after irradiation (Deckbar et al., 2010). This longer damage-insensitive period in G1 versus G2 may be explained by differences in their biochemical pathways. In G1, the DDR involves proteolysis of cyclin D and transcriptional changes such as p53-dependent p21 induction (Waldman et al., 1995; Agami and Bernards, 2000), whereas DDR during G2 inactivates Cdc25, the rate-limiting step for CDK1 activation, through a faster series of phosphorylation and dephosphorylation reactions (Donzelli and Draetta, 2003). From an evolutionary standpoint, we speculate the earlier G1 commitment point from the G1/S transition might be advantageous in delaying DSB repair by the more error-prone non-homologous end-joining in G1 until S or G2, when the more error-free homologous recombination repair option is available (Aylon et al., 2004).

It is important to note that the commitment point that we describe is similar, but not identical, to the concept of a G1 restriction point, a temporal point at which cells in G1 are no longer sensitive to growth factor withdrawal for commitment to S phase entry (Pardee, 1974). Although mediated through different upstream mechanisms, the downstream consequences of serum starvation and DDR both converge on CDK2/4 inactivation (Blagosklonny and Pardee, 2002). Interestingly, the temporal location of the restriction point is comparable with the location of our G1 commitment point mapped 2–3 hr before DNA replication (Campisi et al., 1982), suggesting that different types of cell-cycle checkpoints in G1 may act on a similar timescale due to their converging pathways. However, the DNA damage commitment point we identified is estimated to be earlier than the timing of the point-of-no-return (~0.7 hr before G1/S), which is character-

ized by irreversible APC inactivation (Cappell et al., 2016). However, we do not exclude the possibility that this discrepancy in timing might be explained by the use of different cell lines or methods to measure S phase onset (CDK2 activity versus PCNA foci formation). It is also possible that the location of the point-of-no-return may be stress type-specific, since a lower percentage of cells exit the cell cycle in response to DNA damage compared with oxidative and osmotic stresses (Cappell et al., 2016).

Previous studies that examine radiosensitivity, measured by survival rate after irradiation, also exhibit drastic variation across different cell-cycle phases. Specifically, G2 and M phase cells show the most sensitivity to radiation, followed by G1 cells, with S phase cells being the most resistant to damage (Pawlik and Keyomarsi, 2004). Our results using a radiomimetic drug reveal a similar trend in checkpoint stringencies. The G2 checkpoint is the most stringent, whereas the S phase checkpoint is the least stringent. Therefore, the stringencies of DNA damage checkpoints in each phase seem to be optimized to allow for maximal cell-cycle progression while preventing the lethal consequences of DSBs. Consistent with previous cell-cycle analyses in fixed cells (Nüsse, 1981), S phase progression was minimally affected by damage except for extremely high NCS concentrations (Figures 3A and 3B). Even under the highest levels of damage, cells progressed through S phase and were rarely found to undergo permanent arrest within S phase. The fact that S phase shows the least stringent checkpoint yet is the most resistant to irradiation in terms of viability seems contradictory, since a robust DNA damage checkpoint would be expected to offer the strongest protection from irradiation. However, we found that cells damaged in S phase were arrested in the subsequent G2 phase by comparable or even higher probabilities than cells damaged directly during G2-M (Figures S2C–S2H). This observation suggests that cells damaged in S phase carry incompletely repaired DSBs to G2 and then trigger a robust G2 checkpoint response that protects their viability. Therefore, therapeutically, it might be more effective to target S phase tumor cells when combined with checkpoint inhibitors of G2 rather than inhibitors of S phase progression.

Our work also demonstrates the advantage of using quantitative live-imaging approach to study cell-cycle dynamics. Live-cell imaging measures DNA damage checkpoint dynamics under unperturbed conditions without artificial manipulations such as cell synchronization, which can introduce unwanted DNA damage. Furthermore, the PCNA-based approach also provides an accurate methodology crucial for locating cell-cycle transitions and commitment points (Barr et al., 2016, 2017; Wilson et al., 2016). This method provides an advantage over the widely used fluorescence ubiquitin cell-cycle indicator (FUCCI) system (Dowling et al., 2014; Sandler et al., 2015; Wilson et al., 2016) and its newer version (FUCCI4) (Bajar et al., 2016). Whereas the identification of G1/S transition remained subjective and sensitive to thresholding in FUCCI system and is not capable of sharply demarcating the G1/S transition, the PCNA-based method provides a finer resolution demarcating the boundaries at the G1/S and S/G2 borders (Wilson et al., 2016). Another advantage of using PCNA as a marker of phase transition is its robustness to intensity fluctuation. In the FUCCI system, the demarcation of phase transitions relies on fluorescence intensity, which can

vary under different imaging conditions, expression levels, and fluorophore degradation kinetics. In contrast, phase identification by the PCNA reporter relies on morphological changes due to protein localization that are insensitive to total fluorescence intensity (Zerjatke et al., 2017). Thus, our results provide precise identification of the timing of cell-cycle phase transitions after DNA damage.

Finally, our study reveals meaningful differences between an immortalized primary cell line and a transformed cell line derived from a human tumor. Despite qualitatively similar checkpoint dynamics observed within each phase between RPE and U2OS cells, we find quantitative differences in checkpoint stringencies: diminished checkpoint stringencies in the transformed U2OS cell lines across the cell cycle. This deficiency is most pronounced in G1 (Figures 5C, S2G, and S2H). U2OS cells are known to harbor an unstable G1 checkpoint due to p16 deficiency, truncated Wip1, and p53 heterozygosity (Diller et al., 1990; Stott et al., 1998; Kleiblova et al., 2013). Such diminished G1 checkpoint stringency is attributed to the earlier commitment point relative to the beginning of G1 (Table S2), halt duration upon checkpoint activation (Figure S5B), and diminished ability to permanently arrest cells (Figure S5D). Although both cell lines have a similar duration of the insensitive period after the commitment point, U2OS generally shows a significantly shorter total G1 duration than RPE. Thus, the G1 in U2OS cells has a relatively longer unchecked period compared with the G1 of RPE cells. In addition, our model estimates a better fit for the G1 checkpoint in U2OS with the graded slowdown, as opposed to the all-or-none kinetics seen in RPE cells (Tables S2 and S3). It is possible that this difference in checkpoint kinetics may reflect a more general discrepancy between non-transformed and cancer cells. Graded slowdown kinetics may manifest as the “leakiness” in DNA damage checkpoint responses observed in transformed cells, which has been loosely attributed to defective checkpoint responses (Kastan et al., 1992; Bunz et al., 1998). Thus, in light of cancer treatments that rely on differentially inducing DNA damage, it may be useful to clinically stratify tumors not only based on cell types, but also on the dynamics of DNA damage checkpoint responses.

STAR★METHODS

Detailed methods are provided in the online version of this paper and include the following:

- KEY RESOURCES TABLE
- CONTACT FOR REAGENT AND RESOURCE SHARING
- EXPERIMENTAL MODEL AND SUBJECT DETAILS
 - RPE
 - U2OS
- METHOD DETAILS
 - Cell Culture
 - Cell Line Construction
 - Time-Lapse Microscopy
 - Image Analysis and Quantification
 - In Silico Mapping of Cell Cycle Progression in Individual Cells
 - Immunofluorescence
 - Model Simulations and Parameter Fitting

- QUANTIFICATION AND STATISTICAL ANALYSIS
- DATA AND SOFTWARE AVAILABILITY
 - Software

SUPPLEMENTAL INFORMATION

Supplemental Information includes seven figures, three tables, one data, and two movies and can be found with this article online at <https://doi.org/10.1016/j.cels.2017.09.015>.

AUTHOR CONTRIBUTIONS

H.X.C. and G.D.G. constructed the PCNA-mCherry reporter cell lines. H.X.C. performed validation studies. H.X.C. and J.E.P. designed the experiments. H.X.C., C.E.P., A.A.P., and H.Y.C. performed live-cell imaging and experiments. H.X.C., C.E.P., A.A.P., and H.Y.C. conducted image analysis and cell tracking. H.X.C. performed computational modeling and analysis. H.X.C. wrote the manuscript with contributions from all authors.

ACKNOWLEDGMENTS

We thank Yue Xiong for helpful discussion, Samuel Wolff for guidance on experiments and microscopy operation, Katarzyna Kedziora for critical feedback, Chi Pham for editing the manuscript, and Po-Hao Huang for brainstorming ideas. This work was supported by NIH research grants R00-GM102372 (J.E.P.) and R01-GM102413 (J.G.C.), and R01-GM083024 (J.G.C.); NIH training grants T32CA009156 (G.D.G.), T32-GM067553 (H.X.C.), and F30-CA213876 (H.X.C.); the North Carolina University Cancer Research Fund; and by a medical research grant from the W. M. Keck Foundation (J.E.P. and J.G.C.).

Received: March 27, 2017

Revised: June 26, 2017

Accepted: September 22, 2017

Published: October 25, 2017

REFERENCES

- Agami, R., and Bernards, R. (2000). Distinct initiation and maintenance mechanisms cooperate to induce G1 cell cycle arrest in response to DNA damage. *Cell* 102, 55–66.
- Akan, P., Alexeyenko, A., Costea, P.I., Hedberg, L., Solnestam, B.W., Lundin, S., Hällman, J., Lundberg, E., Uhlén, M., and Lundberg, J. (2012). Comprehensive analysis of the genome transcriptome and proteome landscapes of three tumor cell lines. *Genome Med.* 4, 86.
- Arora, M., Moser, J., Phadke, H., Basha, A., and Spencer, S.L. (2017). Endogenous replication stress in mother cells leads to quiescence of daughter cells. *Cell Rep.* 19, 1351–1364.
- Aylon, Y., Liefshitz, B., and Kupiec, M. (2004). The CDK regulates repair of double-strand breaks by homologous recombination during the cell cycle. *EMBO J.* 23, 4868–4875.
- Bajar, B.T., Lam, A.J., Badiie, R.K., Oh, Y.H., Chu, J., Zhou, X.X., Kim, N., Kim, B.B., Chung, M., Yablonovitch, A.L., et al. (2016). Fluorescent indicators for simultaneous reporting of all four cell cycle phases. *Nat. Methods* 13, 993–996.
- Barr, A.R., Heldt, F.S., Zhang, T., Bakal, C., and Novák, B. (2016). A dynamical framework for the all-or-none G1/S transition. *Cell Syst.* 2, 27–37.
- Barr, A.R., Cooper, S., Heldt, F.S., Butera, F., Stoy, H., Mansfeld, J., Novák, B., and Bakal, C. (2017). DNA damage during S-phase mediates the proliferation-quiescence decision in the subsequent G1 via p21 expression. *Nat. Commun.* 8, 14728.
- Bartek, J., and Lukas, J. (2007). DNA damage checkpoints: from initiation to recovery or adaptation. *Curr. Opin. Cell Biol.* 19, 238–245.
- Blagosklonny, M.V., and Pardee, A.B. (2002). The restriction point of the cell cycle. *Cell Cycle* 1, 102–109.

- Branzei, D., and Foiani, M. (2008). Regulation of DNA repair throughout the cell cycle. *Nat. Rev. Mol. Cell Biol.* **9**, 297–308.
- Bunz, F., Dutriaux, A., Lengauer, C., Waldman, T., Zhou, S., Brown, J.P., Sedivy, J.M., Kinzler, K.W., and Vogelstein, B. (1998). Requirement for p53 and p21 to sustain G2 arrest after DNA damage. *Science* **282**, 1497–1501.
- Burgess, A., Lorca, T., and Castro, A. (2012). Quantitative live imaging of endogenous DNA replication in mammalian cells. *PLoS One* **7**, e45726.
- Campeau, E., Ruhl, V.E., Rodier, F., Smith, C.L., Rahmberg, B.L., Fuss, J.O., Campisi, J., Yaswen, P., Cooper, P.K., and Kaufman, P.D. (2009). A versatile viral system for expression and depletion of proteins in mammalian cells. *PLoS One* **4**, e6529.
- Campisi, J., Medrano, E.E., Morreo, G., and Pardee, A.B. (1982). Restriction point control of cell growth by a labile protein: evidence for increased stability in transformed cells. *Proc. Natl. Acad. Sci. USA* **79**, 436–440.
- Cappell, S.D., Chung, M., Jaimovich, A., Spencer, S.L., and Meyer, T. (2016). Irreversible APCdh1 inactivation underlies the point of no return for cell-cycle entry. *Cell* **166**, 167–180.
- Carpenter, A.E., Jones, T.R., Lamprecht, M.R., Clarke, C., Kang, I.H., Friman, O., Guertin, D.A., Chang, J.H., Lindquist, R.A., Moffat, J., et al. (2006). CellProfiler: image analysis software for identifying and quantifying cell phenotypes. *Genome Biol.* **7**, R100.
- Cortez, D. (2015). Preventing replication fork collapse to maintain genome integrity. *DNA Repair (Amst)* **32**, 149–157.
- Deckbar, D., Stiff, T., Koch, B., Reis, C., Löbrich, M., and Jeggo, P.A. (2010). The limitations of the G1-S checkpoint. *Cancer Res.* **70**, 4412–4421.
- Diller, L., Kassel, J., Nelson, C.E., Gryka, M.A., Litwak, G., Gebhardt, M., Bressac, B., Ozturk, M., Baker, S.J., Vogelstein, B., et al. (1990). p53 functions as a cell cycle control protein in osteosarcomas. *Mol. Cell Biol.* **10**, 5772–5781.
- Donzelli, M., and Draetta, G.F. (2003). Regulating mammalian checkpoints through Cdc25 inactivation. *EMBO Rep.* **4**, 671–677.
- Dowling, M.R., Kan, A., Heinzel, S., Zhou, J.H., Marchingo, J.M., Wellard, C.J., Markham, J.F., and Hodgkin, P.D. (2014). Stretched cell cycle model for proliferating lymphocytes. *Proc. Natl. Acad. Sci. USA* **111**, 6377–6382.
- Elledge, S.J. (1996). Cell cycle checkpoints: preventing an identity crisis. *Science* **274**, 1664–1672.
- Feringa, F.M., Krenning, L., Koch, A., van den Berg, J., van den Broek, B., Jalink, K., and Medema, R.H. (2016). Hypersensitivity to DNA damage in ante-phase as a safeguard for genome stability. *Nat. Commun.* **7**, 12618.
- Ge, X.Q., and Blow, J.J. (2010). Chk1 inhibits replication factory activation but allows dormant origin firing in existing factories. *J. Cell Biol.* **191**, 1285–1297.
- Heijink, A.M., Krajewska, M., and van Vugt, M.A.T.M. (2013). The DNA damage response during mitosis. *Mutat. Res. Mol. Mech. Mutagen.* **750**, 45–55.
- Kastan, M.B., Zhan, Q., el-Deiry, W.S., Carrier, F., Jacks, T., Walsh, W.V., Plunkett, B.S., Vogelstein, B., and Fornace, A.J., Jr. (1992). A mammalian cell cycle checkpoint pathway utilizing p53 and GADD45 is defective in ataxia-telangiectasia. *Cell* **71**, 587–597.
- Kisielewska, J., Lu, P., and Whitaker, M. (2005). GFP-PCNA as an S-phase marker in embryos during the first and subsequent cell cycles. *Biol. Cell* **97**, 221–229.
- Kleiblova, P., Shaltiel, I.A., Benada, J., Ševčík, J., Pecháčková, S., Pohlreich, P., Voest, E.E., Dunder, P., Bartek, J., Kleibl, Z., et al. (2013). Gain-of-function mutations of PPM1D/Wip1 impair the p53-dependent G1 checkpoint. *J. Cell Biol.* **201**, 511–521.
- Krenning, L., Feringa, F.M., Shaltiel, I.A., van den Berg, J., and Medema, R.H. (2014). Transient activation of p53 in G2 phase is sufficient to induce senescence. *Mol. Cell* **55**, 59–72.
- Labib, K. (2010). How do Cdc7 and cyclin-dependent kinases trigger the initiation of chromosome replication in eukaryotic cells? *Genes Dev.* **24**, 1208–1219.
- Lindqvist, A., Rodríguez-Bravo, V., and Medema, R.H. (2009). The decision to enter mitosis: feedback and redundancy in the mitotic entry network. *J. Cell Biol.* **185**, 193–202.
- Müllers, E., Silva Cascales, H., Jaiswal, H., Saurin, A.T., and Lindqvist, A. (2014). Nuclear translocation of Cyclin B1 marks the restriction point for terminal cell cycle exit in G2 phase. *Cell Cycle* **13**, 2733–2743.
- Müllers, E., Silva Cascales, H., Burdova, K., Macurek, L., and Lindqvist, A. (2017). Residual Cdk1/2 activity after DNA damage promotes senescence. *Aging Cell* **16**, 575–584.
- Novak, B., Tyson, J.J., Györfy, B., and Csikasz-Nagy, A. (2007). Irreversible cell-cycle transitions are due to systems-level feedback. *Nat. Cell Biol.* **9**, 724–728.
- Nüsse, M. (1981). Cell cycle kinetics of irradiated synchronous and asynchronous tumor cells with DNA distribution analysis and BrdUrd-Hoechst 33258-technique. *Cytometry* **2**, 70–79.
- Nyberg, K.A., Michelson, R.J., Putnam, C.W., and Weinert, T.A. (2002). Toward maintaining the genome: DNA damage and replication checkpoints. *Annu. Rev. Genet.* **36**, 617–656.
- Orthwein, A., Fradet-Turcotte, A., Noordermeer, S.M., Canny, M.D., Brun, C.M., Strecker, J., Escribano-Diaz, C., and Durocher, D. (2014). Mitosis inhibits DNA double-strand break repair to guard against telomere fusions. *Science* **344**, 189–193.
- Pardee, A.B. (1974). A restriction point for control of normal animal cell proliferation. *Proc. Natl. Acad. Sci. USA* **71**, 1286–1290.
- Paulovich, A.G., and Hartwell, L.H. (1995). A checkpoint regulates the rate of progression through S phase in *S. cerevisiae* in response to DNA damage. *Cell* **82**, 841–847.
- Paulovich, A.G., Toczyski, D.P., and Hartwell, L.H. (1997). When checkpoints fail. *Cell* **88**, 315–321.
- Pawlik, T.M., and Keyomarsi, K. (2004). Role of cell cycle in mediating sensitivity to radiotherapy. *Int. J. Radiat. Oncol. Biol. Phys.* **59**, 928–942.
- Pomerening, J.R., Ubersax, J.A., and Ferrell, J.E., Jr. (2008). Rapid cycling and precocious termination of G1 phase in cells expressing CDK1AF. *Mol. Biol. Cell* **19**, 3426–3441.
- Reinhardt, H.C., and Yaffe, M.B. (2009). Kinases that control the cell cycle in response to DNA damage: Chk1, Chk2, and MK2. *Curr. Opin. Cell Biol.* **21**, 245–255.
- Sandler, O., Mizrahi, S.P., Weiss, N., Agam, O., Simon, I., and Balaban, N.Q. (2015). Lineage correlations of single cell division time as a probe of cell-cycle dynamics. *Nature* **519**, 468–471.
- Shaltiel, I.A., Krenning, L., Bruinsma, W., and Medema, R.H. (2015). The same, only different - DNA damage checkpoints and their reversal throughout the cell cycle. *J. Cell Sci.* **128**, 607–620.
- Sogo, J.M., Lopes, M., and Foiani, M. (2002). Fork reversal and ssDNA accumulation at stalled replication forks owing to checkpoint defects. *Science* **297**, 599–602.
- Soltani, M., Vargas-Garcia, C.A., Antunes, D., and Singh, A. (2016). Intercellular variability in protein levels from stochastic expression and noisy cell cycle processes. *PLoS Comput. Biol.* **12**, e1004972.
- Stott, F.J., Bates, S., James, M.C., McConnell, B.B., Starborg, M., Brookes, S., Palmero, I., Ryan, K., Hara, E., Vousden, K.H., et al. (1998). The alternative product from the human CDKN2A locus, p14(ARF), participates in a regulatory feedback loop with p53 and MDM2. *EMBO J.* **17** (17), 5001–5014.
- Tanaka, S., and Araki, H. (2013). Helicase activation and establishment of replication forks at chromosomal origins of replication. *Cold Spring Harb. Perspect. Biol.* **5**, a010371.
- Taylor, W.R., and Stark, G.R. (2001). Regulation of the G2/M transition by p53. *Oncogene* **20**, 1803–1815.
- Tercero, J.A., and Diffley, J.F.X. (2001). Regulation of DNA replication fork progression through damaged DNA by the Mec1/Rad53 checkpoint. *Nature* **412**, 553–557.
- van Gent, D.C., Hoeyjmakers, J.H., and Kanaar, R. (2001). Chromosomal stability and the DNA double-stranded break connection. *Nat. Rev. Genet.* **2**, 196–206.

- Vilenchik, M.M., and Knudson, A.G. (2003). Endogenous DNA double-strand breaks: production, fidelity of repair, and induction of cancer. *Proc. Natl. Acad. Sci. USA* *100*, 12871–12876.
- Waldman, T., Kinzler, K.W., and Vogelstein, B. (1995). p21 is necessary for the p53-mediated G1 arrest in human cancer cells. *Cancer Res.* *55*, 5187–5190.
- Wang, H., Zhang, X., Teng, L., and Legerski, R.J. (2015). DNA damage checkpoint recovery and cancer development. *Exp. Cell Res.* *334*, 350–358.
- Wilson, K.A., Elefanty, A.G., Stanley, E.G., and Gilbert, D.M. (2016). Spatio-temporal re-organization of replication foci accompanies replication domain consolidation during human pluripotent stem cell lineage specification. *Cell Cycle* *15*, 2464–2475.
- Xu, N., Hegarat, N., Black, E.J., Scott, M.T., Hochegger, H., and Gillespie, D.A. (2010). Akt/PKB suppresses DNA damage processing and checkpoint activation in late G2. *J. Cell Biol.* *190*, 297–305.
- Yekezare, M., Gomez-Gonzalez, B., and Diffley, J.F.X. (2013). Controlling DNA replication origins in response to DNA damage - inhibit globally, activate locally. *J. Cell Sci.* *126*, 1297–1306.
- Zerjatke, T., Gak, I.A., Kirova, D., Fuhrmann, M., Daniel, K., Gonciarz, M., Müller, D., Glauche, I., and Mansfeld, J. (2017). Quantitative cell cycle analysis based on an endogenous all-in-one reporter for cell tracking and classification. *Cell Rep.* *19*, 1953–1966.

STAR★METHODS

KEY RESOURCES TABLE

REAGENT or RESOURCE	SOURCE	IDENTIFIER
Antibodies		
Mouse monoclonal anti-phospho-H2AX Ser139, clone JBW301	EMD Millipore	Cat# 05-636; RRID: AB_309864
Chemicals, Peptides, and Recombinant Proteins		
Neocarzinostatin	Sigma-Aldrich	Cat# N9162
Critical Commercial Assays		
Click-iT EdU kit	Invitrogen	Cat#10337
CellTiter-Blue Cell Viability Assay	Promega	Cat# G8080
Deposited Data		
Raw live-cell movie data	This paper; Mendeley Data	https://doi.org/10.17632/xydd9bvjbz.2 https://doi.org/10.17632/b99nnvft75.1 https://doi.org/10.17632/jzyk4655p.1 https://doi.org/10.17632/gw2hyz54yz.1 https://doi.org/10.17632/dtz2ftpkpw.1 https://doi.org/10.17632/2hw2k2nxh5.1 https://doi.org/10.17632/842zkk6s4v.1 https://doi.org/10.17632/f7nrx8tpf.1 https://doi.org/10.17632/k44t49ct74.1 https://doi.org/10.17632/8y22dnwsxy.1 https://doi.org/10.17632/wm8p7d6gn8.1 https://doi.org/10.17632/dy7ds8htk2.1 https://doi.org/10.17632/yztrdmh4cb.1 https://doi.org/10.17632/gn4gdz6mpy.1 https://doi.org/10.17632/j754858dsb.1 https://doi.org/10.17632/j9tkmrjtd.1 https://doi.org/10.17632/mcfbg64zx2.1 https://doi.org/10.17632/cnbdnrhxm9.1 https://doi.org/10.17632/9zf98p8s7y.1 https://doi.org/10.17632/469p9h3tmc.1 https://doi.org/10.17632/8ydc329gj9.1 https://doi.org/10.17632/zytjrhmpgh.1 https://doi.org/10.17632/6tcms65xjk.1
Experimental Models: Cell Lines		
Human: hTERT retinal pigment epithelial cells (RPE)	ATCC	CRL-4000
Human: U-2 OS	Yue Xiong's Lab	HTB-96
Recombinant DNA		
Plasmid: pLenti-PGK-Puro-TK-NLS-mCherry-PCNA	This paper	N/A
Software and Algorithms		
MATLAB R2015b	The MathWorks Inc. 2010	https://se.mathworks.com/products/matlab.html
Simulations made in MATLAB	This paper	N/A
Cellprofiler	(Carpenter et al., 2006)	http://cellprofiler.org/
Other		
Ti Eclipse inverted microscope	Nikon	https://www.nikoninstruments.com/Products/Inverted-Microscopes/Eclipse-Ti-E
Microscope incubator	okolab	http://www.oko-lab.com/

CONTACT FOR REAGENT AND RESOURCE SHARING

Further information and requests for resources and reagents should be directed to and will be fulfilled by the Lead Contact, Jeremy Purvis (jeremy_purvis@med.unc.edu).

EXPERIMENTAL MODEL AND SUBJECT DETAILS

RPE

hTERT retinal pigment epithelial cells (RPE) were obtained from the ATCC (ATCC[®] CRL-4000[™]) and cultured in DMEM medium supplemented with 10% fetal bovine serum (FBS) and penicillin/streptomycin. The RPE cell line was of female gender source. The cell line was engineered and clonally derived to express PCNA-mCherry (see [Method Details](#) below).

U2OS

U2OS cells were obtained from the laboratory of Dr. Yue Xiong and cultured in McCoy's 5A medium supplemented with 10% fetal bovine serum (FBS) and penicillin/streptomycin (Gibco). The U2OS cell line was of female gender source. The cell line was engineered and clonally derived to express PCNA-mCherry (see [Method Details](#) below).

METHOD DETAILS

Cell Culture

U2OS cells were obtained from the laboratory of Dr. Yue Xiong and cultured in McCoy's 5A medium supplemented with 10% fetal bovine serum (FBS) and penicillin/streptomycin (Gibco). hTERT retinal pigment epithelial cells (RPE) were obtained from the ATCC (ATCC[®] CRL-4000[™]) and cultured in DMEM medium supplemented with 10% fetal bovine serum and penicillin/streptomycin (Gibco). When required, the medium was supplemented with selective antibiotics (2 μ g/mL puromycin (Gibco)). When indicated, medium was replaced with fresh medium supplemented with neocarzinostatin (Sigma-Aldrich) during experiments. Clonogenic assay was performed using the CellTiter-Blue Cell Viability Assay (Promega). Cell cycle distributions were analyzed by DAPI staining and by incorporation of EdU using the Click-iT EdU kit (Invitrogen).

Cell Line Construction

The pLenti-PGK-Puro-TK-NLS-mCherry-PCNA plasmid was subcloned from eGFP-PCNA (Gift from S. Angus) using the Gateway system (Life Technologies) following manufacturers protocols. The eGFP tag from the original plasmid was replaced with mCherry in the pENTR vector intermediate using standard methods. pLenti PGK Puro DEST (w529-2) was a gift from Eric Campeau (Addgene plasmid # 19068)([Campeau et al., 2009](#)). The plasmid was stably expressed into U2OS or RPE cells by first transfecting the plasmid into 293T cells to generate replication-defective viral particles using standard protocols (TR-1003 EMD Millipore), which were used to stably infect the U2OS and RPE cell lines. The cells were maintained in selective media and hand-picked to generate a clonal population.

Time-Lapse Microscopy

Prior to microscopy, cells were plated in poly-D-lysine coated glass-bottom plates (Cellvis) with FluoroBrite[™] DMEM (Invitrogen) supplemented with FBS, 4 mM L-glutamine, and penicillin/streptomycin. Fluorescence images were acquired using a Nikon Ti Eclipse inverted microscope with a Nikon Plan Apochromat Lambda 40X objective with a numerical aperture of 0.95 using an Andor Zyla 4.2 sCMOS detector. In addition, we employed the Nikon Perfect Focus System (PFS) in order to maintain focus of live cells throughout the entire acquisition period. The microscope was surrounded by a custom enclosure (Okolabs) in order to maintain constant temperature (37°C) and atmosphere (5% CO₂). The filter set used for mCherry was: 560/40 nm; 585 nm; 630/75 nm (excitation; beam splitter; emission filter) (Chroma). Images were acquired every 20 mins for U2OS cells and every 10 minutes for RPE cells in the mCherry channel. We acquired 2-by-2 stitched large image for RPE cell. NIS-Elements AR software was used for image acquisition and analysis.

Image Analysis and Quantification

Image analysis was performed using a customized CellProfiler pipeline that included speckle counting and object tracking ([Carpenter et al., 2006](#)), followed by MATLAB (MathWorks) based custom written software to generate the PCNA foci trajectories in [Figures 2E](#) and [2F](#). Specifically, the CellProfiler pipeline utilized the PCNA-mCherry fluorescence channel to segment the nuclei, followed by speckle counting and object tracking to quantify PCNA-mCherry foci over time in each single nuclei. Because the success rate of the CellProfiler's automatic cell tracking was unacceptably low (<20%), mostly due to the mobility of the cells, to obtain higher sample size, we manually tracked each cell and recorded the frame at which PCNA foci appeared (G1/S) or disappeared (S/G2) using ImageJ to produce all the transition curves. Recording of the cell cycle phase transition time frame was performed without blinding. For single-cell studies, cells were naturally randomized in terms of their cell cycle phase and physical position within each experimental condition. The transition curves were constructed from one replication per cell line per treatment condition. Sample sizes (number of cells per experimental condition) for each transition curve ranged between 11 and 160, as indicated in the legend of [Figure 3](#). Sample-size estimation was not performed before data collection. For each experiment, cells that migrated out of the field of microscope view before transitioning and cells that expressed too high fluorescence levels that disallowed confident identification of phase transition time points were excluded from the measurements. All measured cells were included in the analysis. No outliers were excluded.

In Silico Mapping of Cell Cycle Progression in Individual Cells

We quantified the cell cycle phase durations of our cell lines by imaging asynchronously dividing cells. During the entire life of each individual cell, we took four time point measurements: the time of cell birth (t_{birth}), the onset of S phase ($t_{\text{s_onset}}$), the end of S phase ($t_{\text{s_end}}$), and the time of telophase ($t_{\text{telophase}}$) (Figure 2A), which were manually identified from the PCNA-mCherry reporter. These four time points allowed for quantifying the durations of three major cell cycle phases: G1, S, and G2-M phases. For cells with exogenous DNA damage, prior to addition of NCS, we imaged freely cycling cells for at least 15 hours to establish the cell cycle phase duration before the DNA damage was induced.

Immunofluorescence

Cells were fixed and permeabilized with -20°C methanol for 10 minutes, and stained overnight at 4°C with anti-phospho-H2AX Ser139 (JBW301, EMD Millipore 05-636). Primary antibodies were visualized using a secondary antibody conjugated to Alexa Fluor-488/647 and imaged with appropriate filters. EdU incorporation and staining was performed using the Click-iT™ EdU kit (Invitrogen C10337).

Model Simulations and Parameter Fitting

All simulations and parameter fitting were performed using MATLAB. The durations of each cell cycle phase—G1, S, or G2-M—under basal conditions were fitted to an Erlang distribution (Figures S1C and S1D, upper panels). The Erlang distribution was chosen for three main reasons. First, it contains two independent parameters, the minimal number of parameters needed to describe distributions of varying mean and variance. Second, the Erlang distribution has a simple and relevant biological interpretation: each cell cycle phase can be viewed as a multistep biochemical process that needs to be completed sequentially in order to advance to the next cell cycle phase. Alternatively, the multistep process can be viewed as the accumulation of a clock protein whose number needs to exceed a certain threshold value before transitioning to the next cell cycle phase. Third, the Erlang distribution provides a framework that is amenable for carrying out stochastic simulations that are biologically interpretable. In particular, the time step of simulation corresponds to the duration of the current subphase. This framework is also flexible to modifications of the checkpoint dynamics, such as implementing an all-or-none or graded slowdown, as well as introducing a temporally located commitment point within a particular cell cycle phase.

For each cell cycle phase, by fitting the experimental distribution of cell cycle phase durations, we obtained two parameters: shape (k)—which can be interpreted as the number of steps within a cell cycle phase—and scale ($1/\lambda$)—which can be interpreted as the average timescale for each of the steps. After the fitting, we obtained 2 parameters for each cell cycle phase and each cell line. Using the estimated parameters, we were able to simulate the cell cycle phase transitions in an asynchronous population with phase durations drawn from the distribution under basal conditions. In the following, we will use G1 as an example, but the same method was applied to each cell cycle phase. Because the Erlang distribution is a special case of the Gamma distribution with integer scale parameter, we can generate the phase durations from a gamma distribution in MATLAB (Figures S1C and S1D, lower panels):

$$T_{G1,\text{total}} = \sim \text{Gamma}(k, \lambda)$$

Fitting with the “Arrest-and-Restart” Checkpoint Model

Under the arrest-and-restart checkpoint model, the checkpoint implements a complete halt and a permanent arrest probability. Therefore, we incorporated these two properties by introducing two free parameters: delay duration (μ), which was drawn from a normal distribution with standard deviation proportional to the mean, and a permanent arrest probability (p_{arrest}), into our simulations.

$$T_{G1,\text{total}} = \begin{cases} \sim \text{Gamma}(k, \lambda) + t_{\text{halt}}, & \text{with probability } (1 - p_{\text{arrest}}) \\ \infty, & \text{with probability } p_{\text{arrest}} \end{cases}$$

where

$$t_{\text{halt}} \sim \text{Gaussian}(\mu, \mu/3)$$

To simulate cell cycle phase progression in asynchronous cells, we generate a random variable f from 0 to 1 to indicate the proportion of cell cycle phase already completed at the time of damage:

$$f \sim \text{Uniform}(0, 1)$$

With this f , we could then generate the post-damage transition time needed for the transition curves:

$$T_{G1,\text{post-damage}} = \begin{cases} \sim \text{Gamma}(k, \lambda) \times (1 - f) + t_{\text{halt}}, & \text{with probability } (1 - p_{\text{arrest}}) \\ \infty, & \text{with probability } p_{\text{arrest}} \end{cases}$$

We then estimated these two parameters (μ, p_{arrest}) by comparing the simulated transition curve of the model with the experimental data. We used the *fminsearch* function in MATLAB to minimize the mean square difference between the simulation and experimental data in a brute-force approach.

Fitting with the Refined Checkpoint Model

All-or-none Kinetics. In addition to delay duration (μ) and permanent arrest probability (p_{arrest}), as in the arrest-and-restart checkpoint model, we introduced an additional free parameter—commitment point l_{cp} —to allow for checkpoint escape once the cell cycle phase progression passes that temporally located commitment point.

If $f \leq l_{cp}$:

$$T_{G1,total} = \begin{cases} \sim \text{Gamma}(k, \lambda) + t_{halt}, & \text{with probability } (1 - p_{arrest}) \\ \infty, & \text{with probability } p_{arrest} \end{cases}$$

Then, the post-damage transition time would be:

$$T_{G1,post-damage} = \begin{cases} \sim \text{Gamma}(k, \lambda) \times (1 - f) + t_{halt}, & \text{with probability } (1 - p_{arrest}) \\ \infty, & \text{with probability } p_{arrest} \end{cases}$$

If $f > l_{cp}$:

$$T_{G1,total} \sim \text{Gamma}(k, \lambda)$$

Then, the post-damage transition time would be:

$$T_{G1,post-damage} = \sim \text{Gamma}(k, \lambda) \times (1 - f)$$

Graded Slowdown Kinetics. In addition to the above framework that described an all-or-none kinetics, we also performed simulation under the graded slowdown kinetic by allowing the scale parameter (from the fitted Erlang distribution), which related to the rate of progression under basal conditions, to change. Under this graded-slowdown model, we removed the halt duration parameter (μ), and introduced an additional parameter, the new scale, or the phase progression rate after damage (λ_{slow}), to represent the slowed rate after damage.

$$T_{G1,before-damage} \sim \text{Gamma}(k, \lambda) \times f$$

If $f \leq l_{cp}$:

$$T_{G1,post-damage} = \begin{cases} \sim \text{Gamma}(k, \lambda_{slow}) \times (1 - f), & \text{with probability } (1 - p_{arrest}) \\ \infty, & \text{with probability } p_{arrest} \end{cases}$$

If $f > l_{cp}$:

$$T_{G1,post-damage} = \sim \text{Gamma}(k, \lambda) \times (1 - f)$$

Then, the total phase duration would be:

$$T_{G1,total} = T_{G1,before-damage} + T_{G1,post-damage}$$

Although we performed the stochastic simulations under the framework of an Erlang process, it is important to note that the conclusions should be robust to the model framework that we chose. For example, for the all-or-none checkpoint kinetics, the halt durations in G2-M were apparent in the plateau region of the transition curve and did not depend on whether it was an Erlang process. For the graded slowdown checkpoint kinetics in S phase, the slowed cell cycle phase progression could be estimated by calculating the slope as in Figure 6B, which is independent of the model framework. These parameters could be estimated under a deterministic framework. However, the Erlang process provided an easy and trackable framework to carry out the stochastic simulations with modifications upon DNA damage.

QUANTIFICATION AND STATISTICAL ANALYSIS

Statistical parameters including the exact value of n , the definition of center, dispersion and precision measures (mean \pm SEM) and statistical significance are reported in the Figures and Figure Legends. Data is judged to be statistically significant when $p < 0.05$ by Fisher's exact test or the Kolmogorov-Smirnov test as indicated in the Figure Legends. Statistical analysis was performed in MATLAB.

DATA AND SOFTWARE AVAILABILITY

Software

All simulations and data-analysis were performed using custom scripts written in MATLAB, R2015b. The script that generates the simulations is provided in the supplemental files (Data S1). All scripts used for simulation and data analysis from the model will be available upon request to Sherry Chao (hchao@email.unc.edu). The raw images have been deposited in Mendeley Data under ID codes <https://doi.org/10.17632/xydd9bvjbz.2>, <https://doi.org/10.17632/b99nnvft75.1>, <https://doi.org/10.17632/jzyk4655p.1>, <https://doi.org/10.17632/gw2hyz54yz.1>, <https://doi.org/10.17632/dtz2ftpkpw.1>, <https://doi.org/10.17632/2hw2k2nxh5.1>, <https://doi.org/10.17632/>

842zkk6s4v.1, <https://doi.org/10.17632/f7nrx8tpf.1>, <https://doi.org/10.17632/k44t49ct74.1>, <https://doi.org/10.17632/8y22dnwsxy.1>, <https://doi.org/10.17632/wm8p7d6gn8.1>, <https://doi.org/10.17632/dy7ds8htk2.1>, <https://doi.org/10.17632/yztrdmh4cb.1>, <https://doi.org/10.17632/gn4gdz6mpy.1>, <https://doi.org/10.17632/j754858dsb.1>, <https://doi.org/10.17632/j9tkrmrjtd.1>, <https://doi.org/10.17632/mcfbg64zx2.1>, <https://doi.org/10.17632/cnbdnrhxm9.1>, <https://doi.org/10.17632/9zf98p8s7y.1>, <https://doi.org/10.17632/469p9h3tmc.1>, <https://doi.org/10.17632/8ydc329gj9.1>, <https://doi.org/10.17632/zytjrhmpgh.1>, and <https://doi.org/10.17632/6tcms65xjk.1>. Example raw live images are provided in the supplemental file ([Movies S1](#) and [S2](#)).

Cell Systems, Volume 5

Supplemental Information

Orchestration of DNA Damage Checkpoint

Dynamics across the Human Cell Cycle

Hui Xiao Chao, Cere E. Poovey, Ashley A. Privette, Gavin D. Grant, Hui Yan Chao, Jeanette G. Cook, and Jeremy E. Purvis

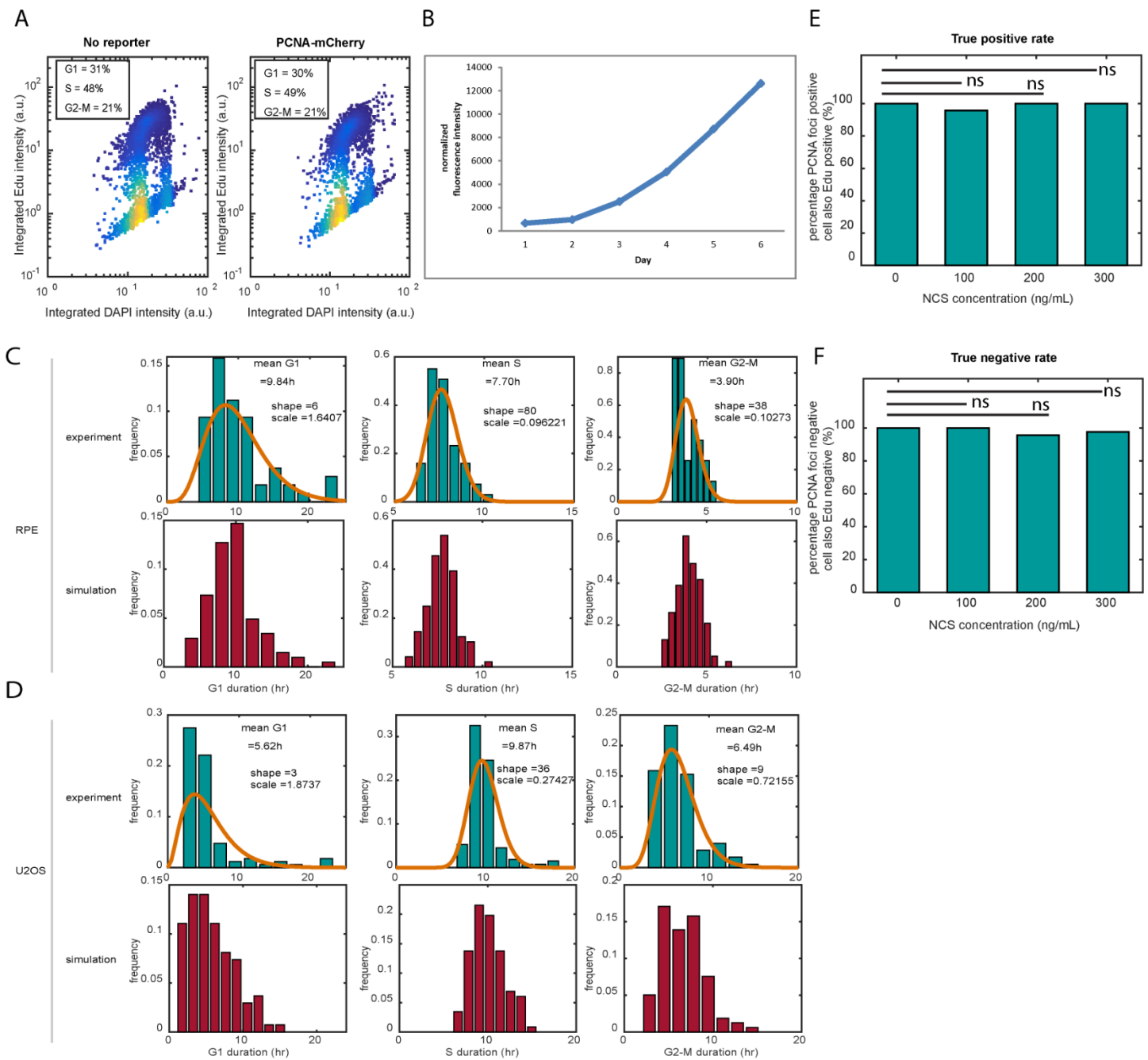


Figure S1. Related to Figure 2. Characterization of cell cycle progression by the PCNA-mCherry reporter.

A. Cell cycle distribution of U2OS cells. Cells with (left panel) and without (right panel) the expression of PCNA-mCherry were pulsed with 10 μ M EdU for 1 hour, followed by fixation, staining, and quantification for EdU incorporation and DAPI content. The colors represent the density of data points: yellow, high density; blue, low density. ($n > 1800$)

B. The doubling time of the cell line in culture was consistent with the cell cycle durations measured from live-cell image. The doubling time (20.1 hours) of U2OS cells expressing the PCNA-mCherry reporter was measured by fitting the most rapid phase of the growth curve with an exponential function. Relative cell count was quantified using the CellTiter blue assay.

C-D. Top panels: Asynchronously proliferating RPE (C) and U2OS (D) cells were quantified for their cell cycle phase (G1, S, G2-M) durations based PCNA-mCherry morphology using time-lapse microscopy. The distributions of the cell cycle phase were fitted with Erlang distributions to estimate the shape (k) and scale ($1/\lambda$) parameters. Bottom panels: simulations of cell cycle phase durations based on the fitted Erlang distribution parameters. $n > 60$, except for RPE G2-M $n = 26$.

E-F. The true positive rate (E) and true negative rate (F) of the PCNA foci as a marker for S phase, measured by EdU incorporation. U2OS cells were treated with NCS of indicated concentrations under live-cell imaging conditions to quantify for PCNA foci. 10 hours after the treatment, the cells were pulsed with 10 μ M EdU for 20 mins, followed by fixation, staining, and scoring for EdU incorporation. ns indicates no significant difference based on the significance level of $p = 0.05$ using Fisher's exact test. In addition, DNA damage-induced PCNA foci in G1 or G2 were not observed under our conditions, which could cause the cells to be erroneously scored as having entered S phase. ($n > 65$)

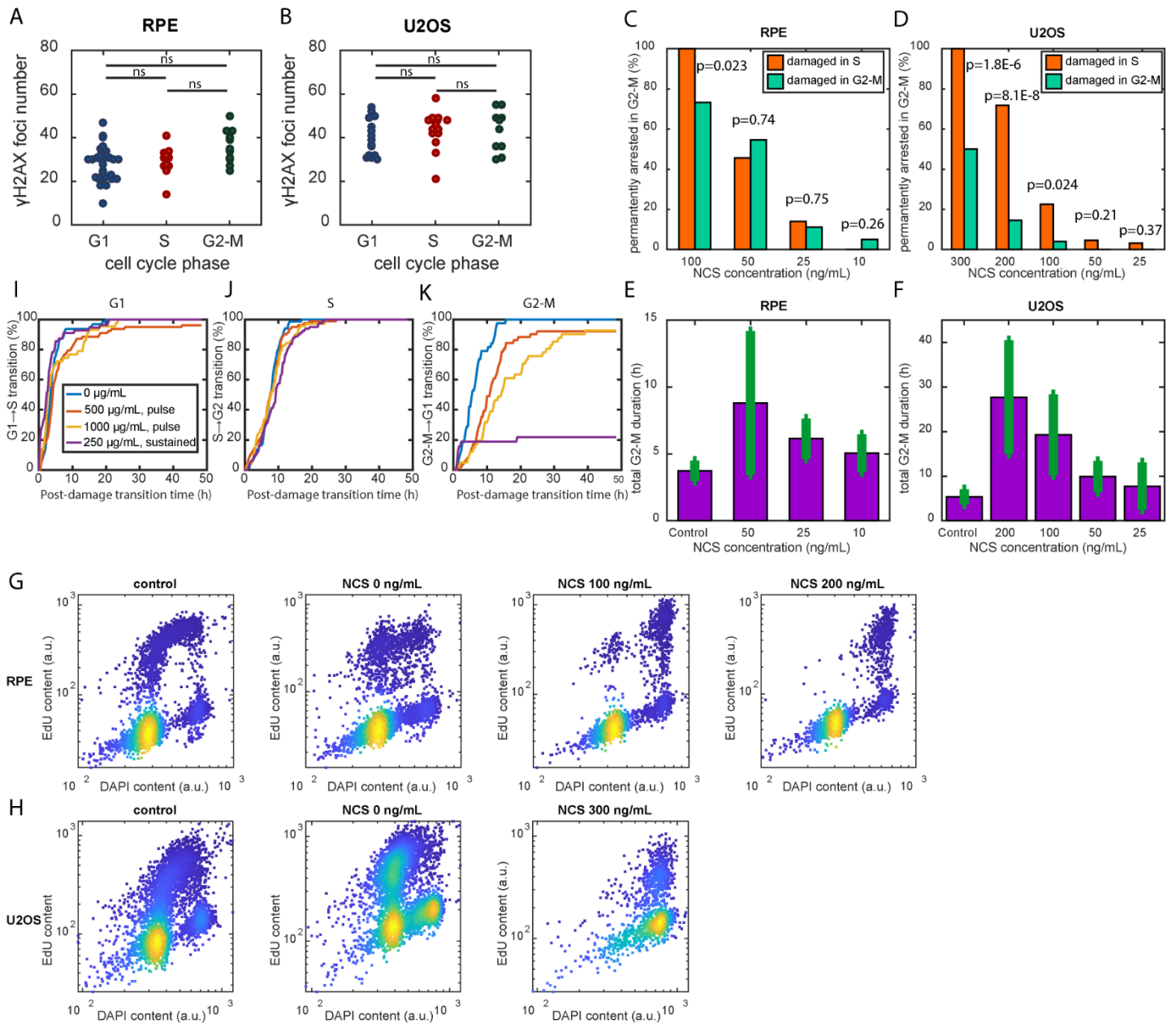


Figure S2. Related to Figure 3. Quantifying the effects of DNA damage on cell cycle progression.

A-B. RPE (A) and U2OS (B) cells were induced with 100 ng/mL and 300 ng/mL NCS, respectively, for 30 minutes, and pulsed with 10 μM EdU for 15 minutes before fixation. The cells were then stained for γH2AX and DAPI to quantify the level of DSBs and DNA content, respectively. The cell cycle phase was designated based on the EdU and DAPI intensity. ns indicates no significant difference, based on the significance level of $p=0.05$ using Kolmogorov–Smirnov test.

C-D. RPE (C) and U2OS (D) cells that were damaged in S and G2-M were quantified for the fractions of being arrested in G2-M by the end of 48hr hour post damage. The p-values were calculated based on Fisher's exact test.

E-F. RPE (E) and U2OS (F) cells that were damaged in S and completed the subsequent G2-M were quantified for the G2-M durations. Control represents cells without NCS treatment. Error bars represent standard deviations.

G-H. Measuring the fate of cells damaged in S phase. RPE (G) and U2OS (H) cells were treated with NCS of indicated concentrations for 5 mins, followed by a pulse of 10 μ M EdU for 25 mins, and then washed out with fresh media. The cells were then incubated for 20 hours to allow for cell cycle progression before fixation, staining, and quantification for EdU incorporation and DAPI content. The cells in the control were not treated with NCS and were pulsed with 25 minutes of EdU right before fixation to reveal the cell cycle distribution in unperturbed cells. The colors represent the density of data points: yellow, high density; blue, low density. (n ranges from 1300 to 5000)

I-K. Cell cycle phase-specific transition curves in response to zeocin damage in U2OS cells. Transition curves for asynchronously dividing U2OS cells treated with either a 10-minute pulse of zeocin at 500 μ g/mL and 1000 μ g/mL or sustained zeocin at 250 μ g/mL during (I) G1, (J) S, or (K) G2-M. The pulse treatment was used to generate the transient DNA damage effect as NCS. The sustained treatment was used to generate long-term DNA damage.

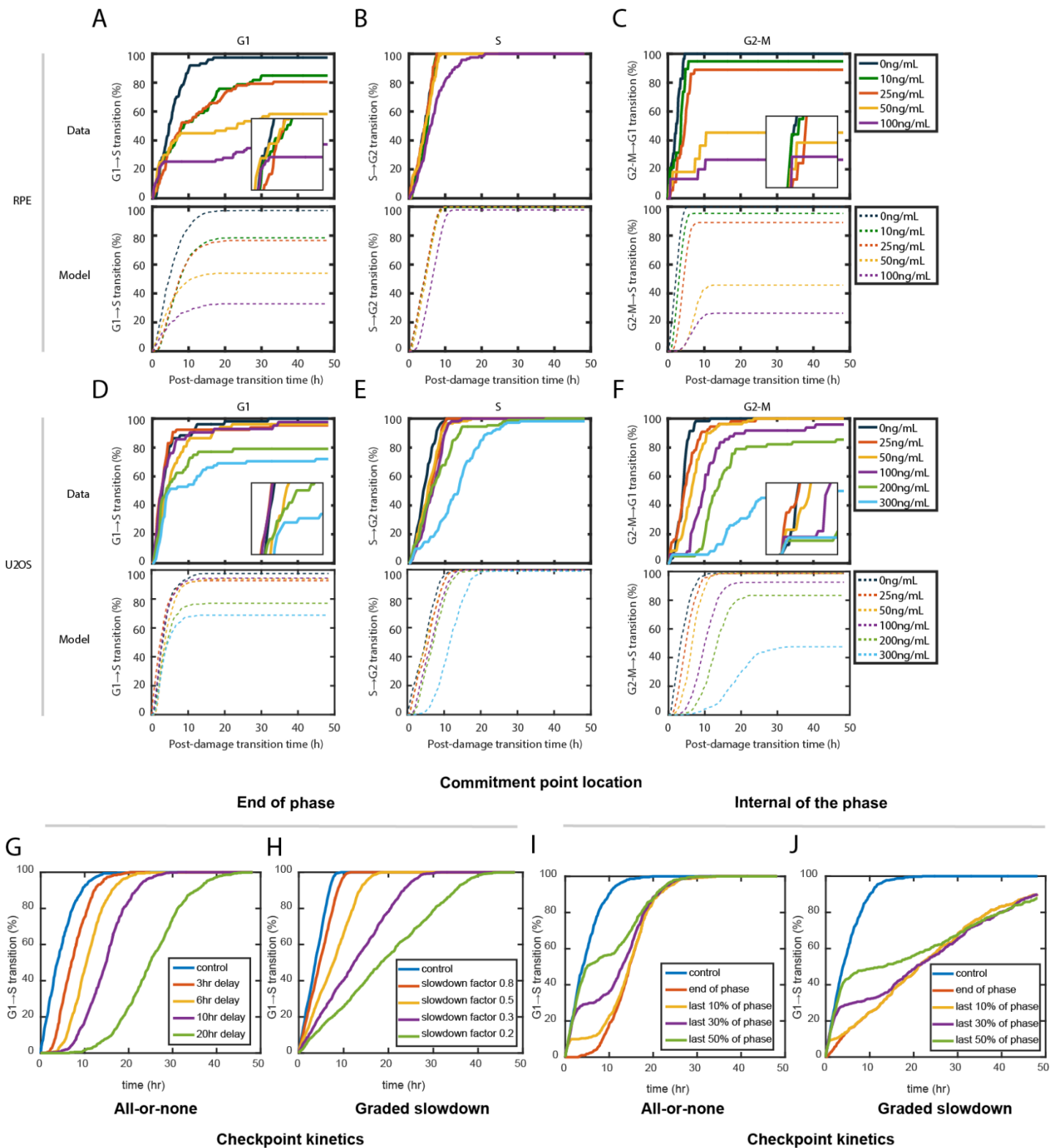


Figure S3. Related to Figure 3. Each cell cycle phase implements a distinct DNA damage checkpoint response.

A-C. Cell cycle phase-specific transition curves in response to acute DNA damage in RPE cells. *Upper panels and solid lines*: As in **Figure 3A-B**, transition curves for asynchronously dividing RPE treated with NCS at the indicated concentrations during (A) G1, (B) S, or (C) G2-M. *Lower panels and dashed lines*: Best fit lines of the experimental data to the “arrest-and-restart” DNA damage checkpoint model described in **Figure 1A**.

D-F. Corresponding experimental data and model fitted curves for U2OS cells as described in panels A-C.

G-H. Simulation of cell cycle transition dynamics upon DNA damage under (G) all-or-none kinetics with varying halt duration, or (H) graded slowdown kinetics with varying slowdown factor.

I-J. Simulation of the cell cycle transition dynamics as in G and H, but incorporating the commitment point at varying locations. For the all-or-none kinetics (I), the delay was set to 10 hours. For the graded slowdown kinetics (J), the slowdown factor was set to 0.2.

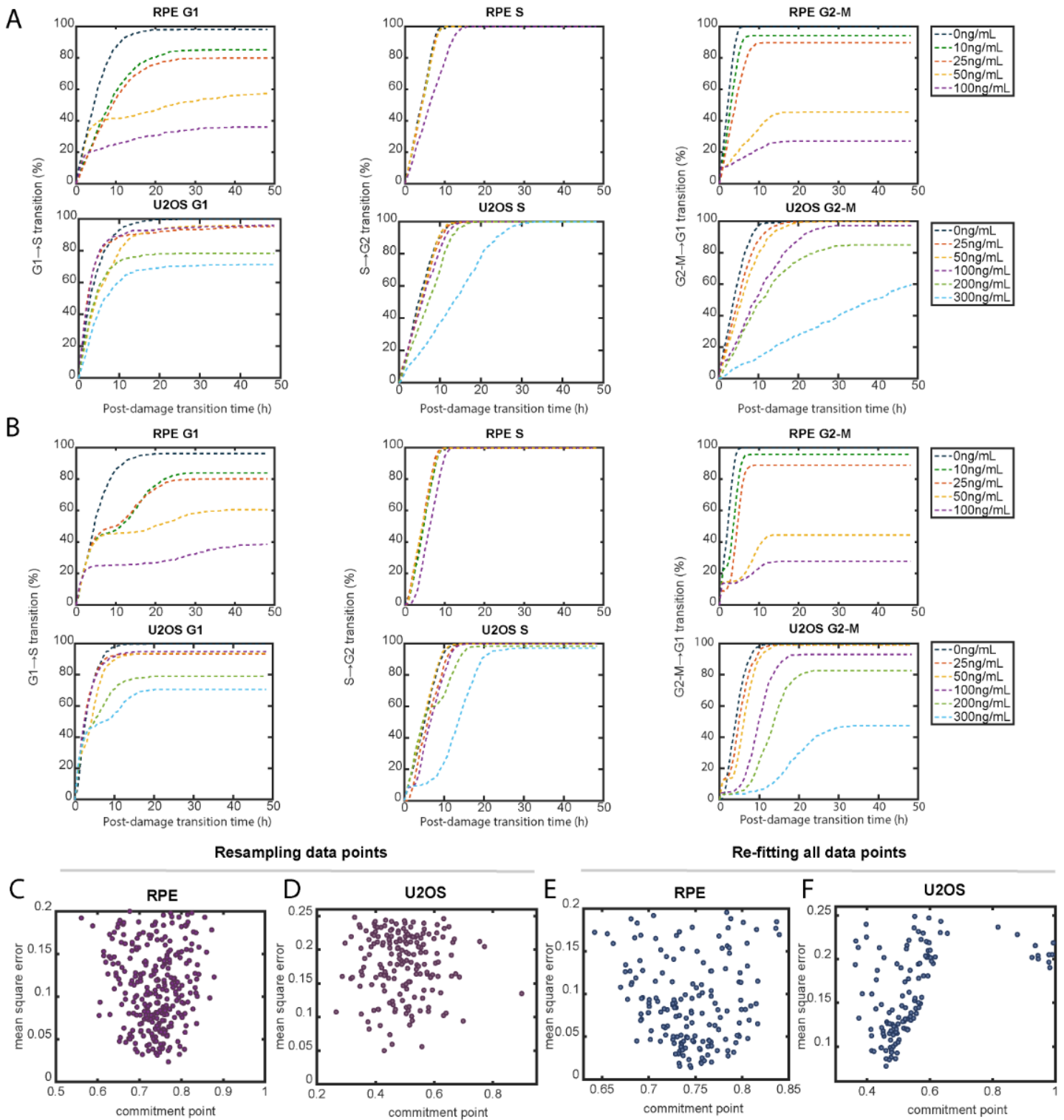


Figure S4. Related to Figure 3. Model fitting of the cell cycle phase-specific transition curves in response to acute DNA damage.

A-B. Model fitting of cell cycle phase-specific transition curves in response to acute DNA damage, as in lower panels of **Figure S3A-F**, but fit with the refined model that incorporated both the flexible commitment point location and the possibility of graded slowdown checkpoint kinetics. Each condition was fit with the (A) graded slowdown or (B) all-or-none checkpoint kinetics.

C. Commitment point estimation by resampling half of the transition data. The transition time points for RPE's G1 transition curve under 100 ng/mL NCS treatment were repeatedly and randomly drawn using half of the data points (n=51) and were fitted with the refined all-or-none checkpoint model. Estimated parameters that produced a simulated transition curve with a mean square error less than 0.2 from the experimental data were recorded (n=294).

D. Same as C, but with U2OS's G1 transition curve under 300 ng/mL NCS and half sample size of 31. Estimated parameters that produced a simulated transition curve with a mean square error less than 0.25 from the experimental data were recorded (n=181).

E. Commitment point estimation by repeated fitting using all of the transition data. The transition time points for RPE's G1 transition curve under 100 ng/mL NCS treatment were repeatedly fitted with the refined all-or-none checkpoint model. Estimated parameters that produced a simulated transition curve with a mean square error less than 0.2 from the experimental data were recorded (n=166).

F. Same as E, but for U2OS's G1 transition curve under 300 ng/mL NCS. Estimated parameters that produced a simulated transition curve with a mean square error less than 0.25 from the experimental data were recorded (n=126).

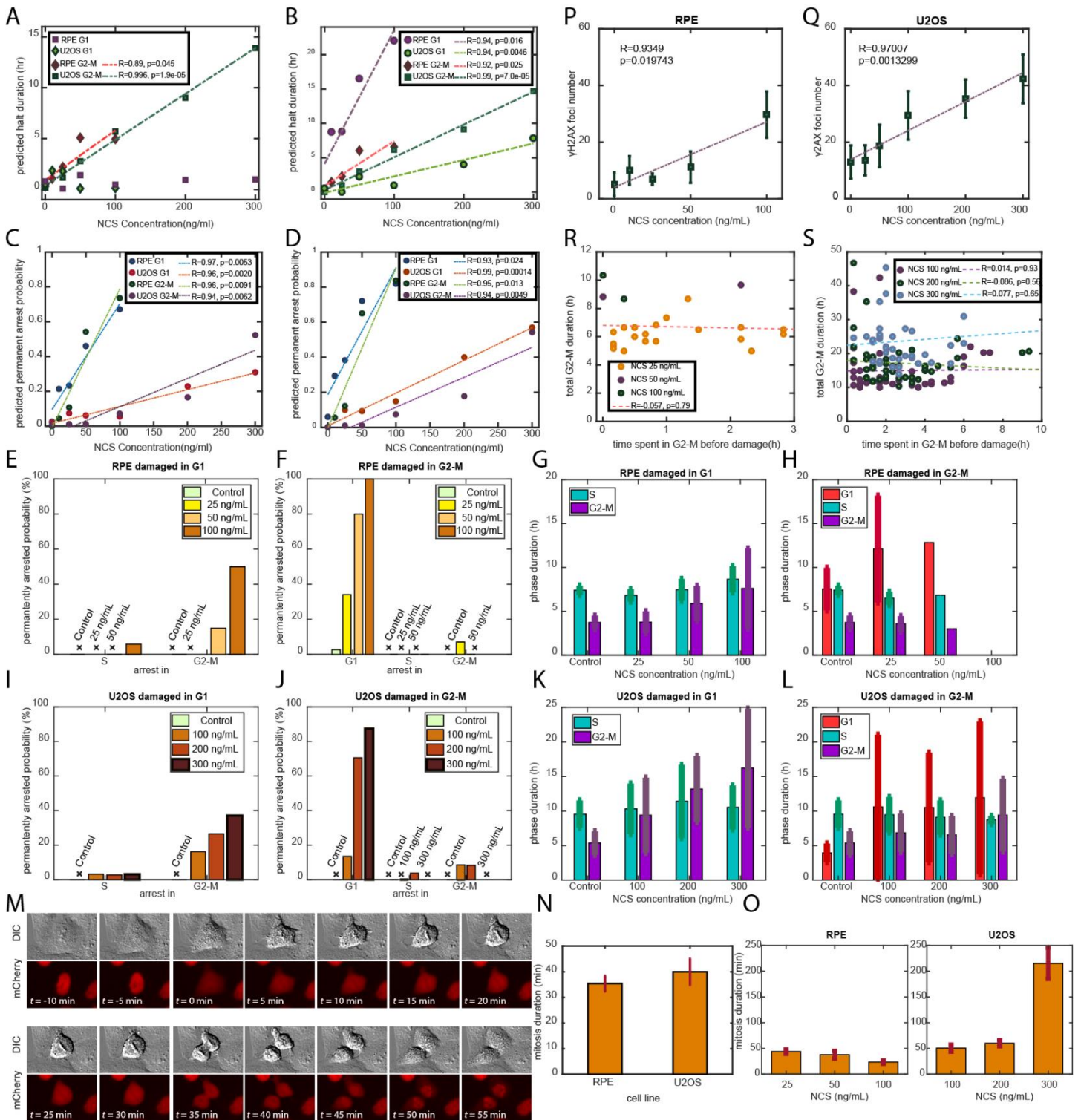


Figure S5. Related to Figure 4. Cell cycle phase-specific checkpoint dynamics and subsequent cell fate as a function of DNA damage level.

A. By fitting the data with the “arrest-and-restart” model, we estimated the halt durations in G1 and G2-M in response to the indicated NCS concentrations.

B. Same as A, but the data were fitted with the refined model with a flexible commitment point.

C. By fitting the data with the “arrest-and-restart” model, we estimated the permanent arrest probabilities in G1 and G2-M in response to the indicated NCS concentrations.

D. Same as C, but the data were fitted with the refined model with a flexible commitment point.

E-F. RPE cells damaged in (E) G1 and (F) G2-M that eventually transitioned to the next phase were quantified for the probability of being arrested in the subsequent phases by the end of the 48-hour experiment. The probability of permanent arrest in a given phase was conditioned on the cells that had entered that given phase. The “x” symbols indicate 0% permanent arrest.

G-H. RPE cells damaged in (G) G1 and (H) G2-M and completed the subsequent cell cycle phases were quantified for the phase durations. (G) For cells damaged in G1, the subsequent S (n= 42, 22,16) and G2-M (n=40, 17, 5) durations were quantified. (H) For cells damaged in G2-M, the G1 (n=22, 1, 0), S (n=16, 1, 0), and G2-M (n=15, 1, 0) durations of the daughter cells were quantified (n values corresponded to NCS 100 ng/mL, 200 ng/mL, 300 ng/mL). Control represents cells without NCS treatment. Error bars represent standard deviations.

I-J. Same as in E-F, but with U2OS cells.

K-L. Same as in G-H, but with U2OS. (K) For cells damaged in G1, the subsequent S (n=31, 36, 32) and G2-M (n=26, 25, 17) durations were quantified. (L) For cells damaged in G2-M, the G1 (n=51, 28, 8), S (n=38, 25, 6), and G2-M (n=32, 11, 5) durations of the daughter cells were quantified (n values corresponded to NCS 100 ng/mL, 200 ng/mL, 300 ng/mL).

M. Live-cell images of a single U2OS cell undergoing mitosis. Upper row: differential interference contrast (DIC). Lower row: mCherry channel. t represents the time since the onset of mitosis, identified by cell rounding and nuclear envelope breakdown.

N. Mitosis durations based on nuclear envelope breakdown revealed by both DIC and mCherry channels under basal conditions. The error bars represent standard error of mean (n=10).

O. Mitosis durations based on nuclear envelope breakdown revealed by both the DIC and mCherry channels under basal conditions. The error bars represent standard error of mean (RPE: n=31 (25 ng/mL), 4 (50 ng/mL), 3 (100 ng/mL). U2OS: n>32 in all conditions).

P-Q. Asynchronous RPE (P) and U2OS (Q) cells were treated with the indicated concentrations of NCS. After 60 minutes, cells were fixed, stained, and quantified for γ H2AX foci. The data were fitted with a linear regression. The error bars represent standard error of the mean.

R-S. RPE (R) and U2OS (S) cells were treated with the indicated NCS concentrations and followed for phase transitions. The total G2-M durations of those that were prolonged were plotted against the time spent in G2-M before damage. The data were fitted with a linear regression. The data for RPE under 50 ng/mL and 100 ng/mL were not fitted with linear regression separately, due to the small sample size.

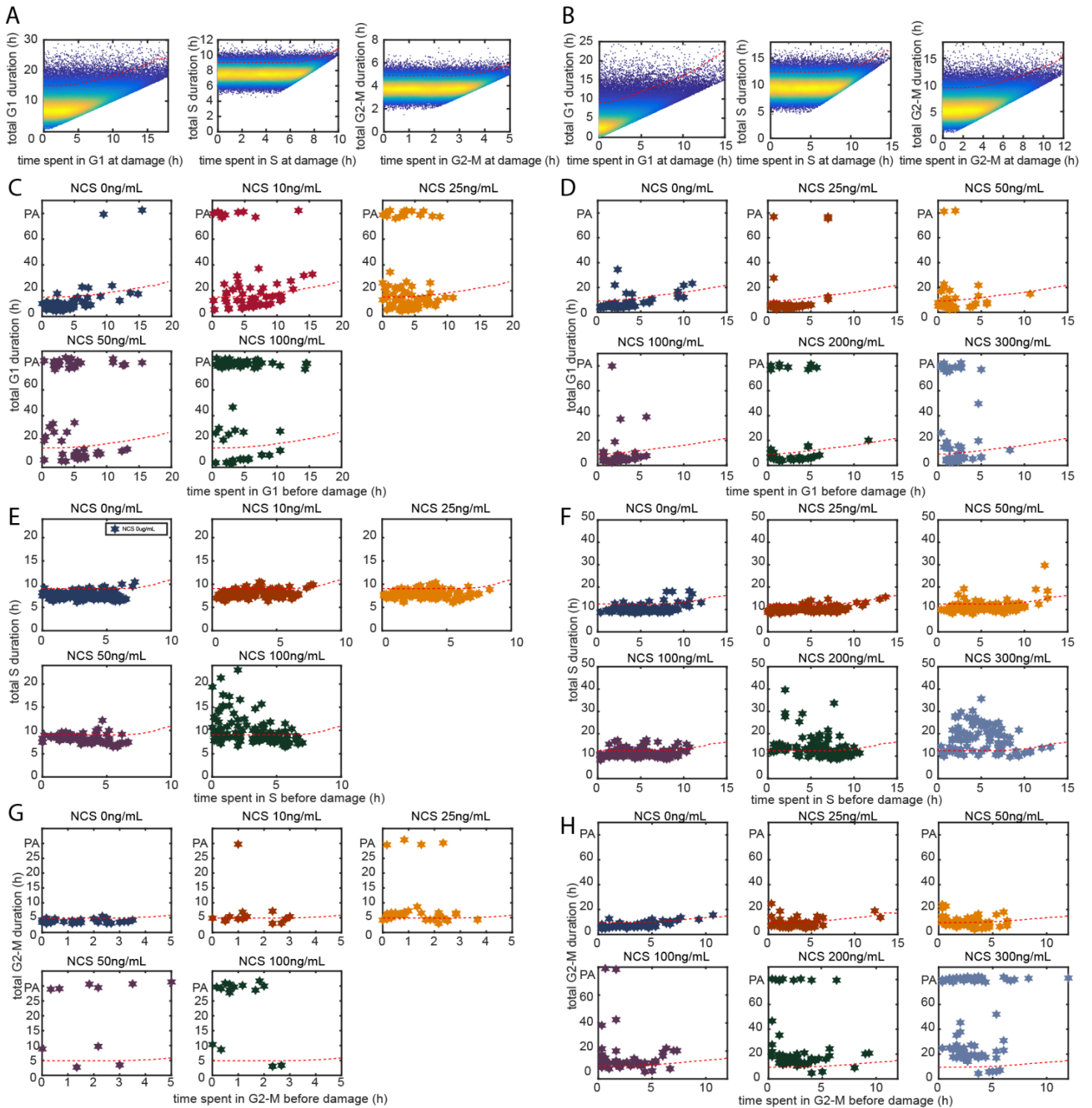


Figure S6. Related to Figure 5. Cell cycle response as a function of cell cycle progress into the phase of damage.

A-B. Simulation of cell cycle phase duration produced the 95 percentile cell cycle. Simulation parameters were obtained from the untreated controls' cell cycle phase durations of (A) RPE and (B) U2OS, fitted with the Erlang distribution. Each point represents a single simulated cell, and the colors represent the density of data points. The red dashed lines represent the top 95 percentile of the total S phase duration for a given time spent in that phase at damage.

C-H. The total cell cycle phase durations of RPE (C, E, G) and U2OS (D, F, H) cells were plotted against the time spent in that phase at the time of damage. The 95 percentile lines (red dashed lines) obtained from **Figure S6A-B** were superimposed onto these plots. This analysis allows for the designation each cell into the three outcome categories (unaffected, temporary arrest, and permanent arrest), as in **Figure 5B**. PA indicates permanent arrest.

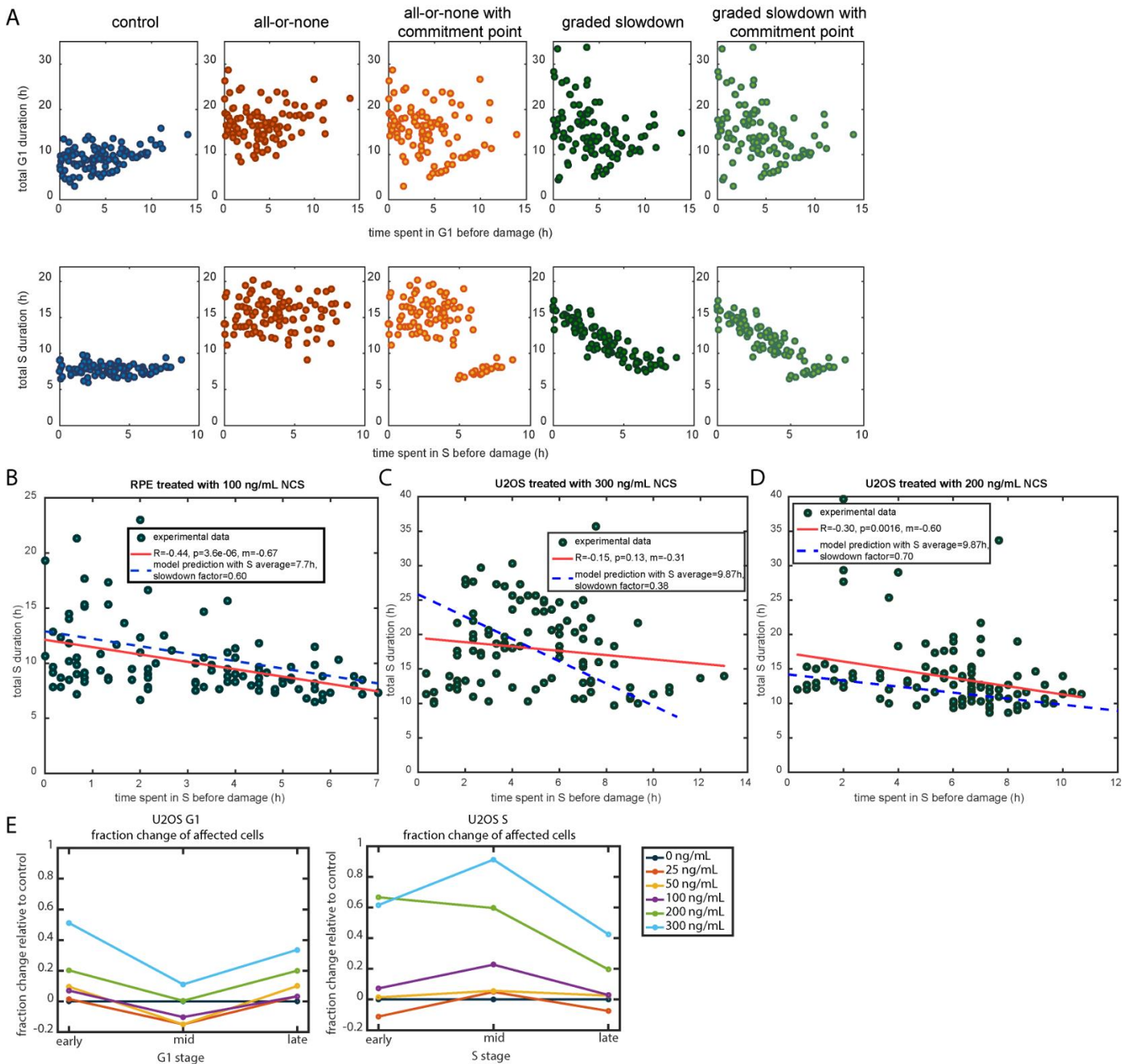


Figure S7. Related to Figure 6. The timing of DNA damage within cell cycle phase affects the cell cycle outcomes.

A. Simulations of cell cycle phase durations as a function of time spent in that phase before damage. Simulations were performed using the fitted parameters (the shape, k , and scale, $1/\lambda$) from RPE's G1 (upper panels) and S phase (lower panels) distributions to represent a phase duration with large variance and small variance, respectively. In the cases with all-or-none checkpoint kinetics, the delay duration was 8 hours. In the cases of graded slowdown checkpoint kinetics, the slowdown factor was 0.5. In the cases of an internal commitment point, the location was 75% of the entire phase from the onset of the phase.

B-D. Experimental data of the total S phase durations as a function of time spent in S phase before damage. Data were from RPE (B) and U2OS (C-D) cells treated with NCS concentrations high enough to affect the total

S phase durations. Red lines represent linear regression of the experimental data. Blue dash lines represent the model predictions of the mean S phase durations based on the graded slowdown checkpoint kinetics.

E. Cell cycle outcome's dependency on the stage of cell cycle phase progression, as in **Figure 6C**. Cell cycle outcomes are plotted as a function of cell cycle phase stage—early, mid, and late stages. Early, mid, and late stages were categorized based on thresholds defined by the 33 and 67 percentiles of time spent in a phase at the time of damage. Fraction change relative to control was obtained by calculating the difference between the fraction of cells being affected (either temporary or permanent arrest) under NCS treatment and that without NCS treatment. The construction of such cell cycle phase stage plot in RPE's G2-M could not be performed due to the short length of G2-M duration and sparsity of cells (see **Figure S6G**). The increased affected fraction in late G1 stage can be explained by sampling bias, such that cells categorized as late stage were possibly already activating arrest response before NCS treatment. Therefore, there is a strong dependency of total duration on the stage during which the cell is sampled, as seen in **Figure S6B** left panel.

Table S1. Related to Figure 3. Fitting parameters for the “arrest-and-restart” checkpoint model reveal dependencies of halt duration and permanent arrest probability on damage level.

G1			
	NCS (ng/mL)	time delay (h)	permanent arrest probability
RPE	0	0.4932	0.0252
	10	1.8399	0.2147
	25	1.7891	0.2333
	50	0.0864	0.4596
	100	0.1242	0.6717
U2OS	0	0.7872	0.0221
	25	0.075	0.0738
	50	1.3993	0.0611
	100	0.4638	0.0553
	200	9.31E-01	0.2281
	300	0.9816	0.311
S			
	NCS (ng/mL)	time delay (h)	permanent arrest probability
RPE	0	0.4093	0.0028
	10	0.5294	0.0042
	25	0.2848	2.96E-04
	50	0.7645	9.34E-04
	100	2.3355	0.0213
U2OS	0	3.06E-04	1.79E-04
	25	4.89E-01	5.47E-05
	50	0.5125	1.87E-04
	100	1.8002	2.49E-04
	200	2.2	0.0099
	300	6.75	0.0093
G2-M			
	NCS (ng/mL)	time delay (h)	permanent arrest probability
RPE	0	0.3022	3.59E-04
	10	1.0622	0.0456
	25	2.1987	0.1081
	50	5.0812	0.5414
	100	4.9552	0.7361
U2OS	0	4.98E-01	0.0104
	25	1.6519	0.0105
	50	3.4003	0.0112
	100	6.5444	0.0726
	200	9.3505	0.1656
	300	0.9816	0.311

Table S2. Related to Figure 3. The refined checkpoint model with all-or-none kinetics improves fits for the gap-phase checkpoints.

G1					
	NCS (ng/mL)	time delay (h)	permanent arrest probability	commitment point (fraction from phase onset)	difference between data and model
RPE	0	0.5059	0.0592	0.6047	0.074
	10	8.7336	0.2941	0.5104	0.2291
	25	8.8012	0.3824	0.5084	0.3027
	50	16.5	0.72	0.52	0.0547
	100	22.0196	0.818	0.7484	0.0351
U2OS	0	5.29E-01	2.13E-05	0.9496	0.1222
	25	9.04E-05	0.0993	0.6333	0.0542
	50	2.2204	0.0922	0.6758	0.1748
	100	0.9751	0.1489	0.3506	0.0933
	200	4.00E+00	0.4	0.5139	0.0879
	300	7.8327	0.5694	0.5036	0.249
S					
	NCS (ng/mL)	time delay (h)	permanent arrest probability	commitment point (fraction from phase onset)	difference between data and model
RPE	0	0.5988	0.0026	0.9648	0.0195
	10	0.7661	1.20E-03	0.9976	0.1123
	25	0.3742	1.40E-03	9.99E-01	3.82E-02
	50	0.6504	1.40E-03	9.98E-01	2.82E-02
	100	2.3799	9.54E-04	0.9974	0.52
U2OS	0	2.23E-05	1.89E-05	0.7009	0.0823
	25	1.05E+00	8.77E-20	1.00E+00	3.98E-02
	50	8.42E-08	1.01E-02	0.0967	0.016
	100	1.9833	1.53E-04	0.8988	0.0371
	200	4.0074	0.04	0.4002	0.1035
	300	8.5809	0.031	0.897	0.1367
G2-M					
	NCS (ng/mL)	time delay (h)	permanent arrest probability	commitment point (fraction from phase onset)	difference between data and model
RPE	0	0.2606	1.40E-03	0.7178	0.0258
	10	1.45	0.0543	0.7621	0.0723
	25	2.294	0.121	0.9057	0.0667
	50	6.0419	0.651	0.8184	0.0642
	100	6	0.81	0.88	0.0551
U2OS	0	1.05E+00	2.50E-04	0.9995	0.0932
	25	1.9333	9.70E-03	8.53E-01	0.0547
	50	3.2045	1.00E-02	0.8774	0.0575
	100	6.58	0.0731	0.9554	0.0706
	200	9.3695	0.178	0.9573	0.0554
	300	15.1824	0.5423	0.9587	0.0308

Table S3. Related to Figure 3. The refined checkpoint model with graded slowdown kinetics improves fits for the S phase checkpoint.

G1					
	NCS (ng/mL)	slowdown factor	permanent arrest probability	commitment point (fraction from phase onset)	difference between data and model
RPE	0	0.952	0.0191	0.9999	0.0487
	10	0.5832	0.157	0.9581	0.2804
	25	0.5795	0.2008	0.9998	0.1297
	50	0.2573	0.6969	0.594	0.0868
	100	0.3313	0.7971	0.7878	0.076
U2OS	0	0.71	1.25E-04	0.9999	0.1167
	25	0.1112	0.194	0.0989	0.0425
	50	0.5121	0.047	0.8961	0.0487
	100	0.2093	2.95E-01	0.0978	0.039
	200	6.80E-01	0.2175	0.9999	0.0479
300	0.51	0.288	0.9998	0.1006	
S					
	NCS (ng/mL)	slowdown factor	permanent arrest probability	commitment point (fraction from phase onset)	difference between data and model
RPE	0	0.95	2.30E-04	0.9699	0.0362
	10	0.9077	9.21E-05	0.9705	0.2602
	25	0.9061	2.50E-04	9.70E-01	6.66E-02
	50	0.9059	2.70E-04	9.70E-01	2.51E-02
	100	0.5971	3.76E-04	0.9614	0.119
U2OS	0	0.9022	2.50E-04	0.1015	0.1106
	25	0.9	5.72E-08	1.00E+00	5.48E-02
	50	0.9015	5.84E-05	0.8971	0.0202
	100	0.8076	4.48E-07	0.9	0.0695
	200	0.6952	1.49E-05	0.9998	0.0826
300	0.3823	3.34E-04	0.9997	0.1123	
G2-M					
	NCS (ng/mL)	slowdown factor	permanent arrest probability	commitment point (fraction from phase onset)	difference between data and model
RPE	0	0.9042	1.25E-05	0.99	0.0284
	10	0.6929	0.0599	0.9488	0.1943
	25	0.5034	0.104	0.9999	0.1751
	50	0.2945	0.6061	0.8974	0.1301
	100	0.2855	0.8166	0.8792	0.0631
U2OS	0	0.7979	2.59E-04	0.9999	0.2536
	25	0.604	2.08E-04	0.9023	0.043
	50	0.4904	1.44E-04	1.00E+00	0.1152
	100	0.3144	0.0292	0.8998	0.5278
	200	0.3103	0.1499	1	0.9916
300	0.0994	0.25	1	0.3046	